

NGTS-28Ab: A short period transiting brown dwarf

Beth A. Henderson¹ *, Sarah L. Casewell¹, Michael R. Goad¹, Jack S. Acton¹, Maximilian N. Günther², Louise D. Nielsen³, Matthew R. Burleigh¹, Claudia Belardi¹, Rosanna H. Tilbrook¹, Oliver Turner⁴, Steve B. Howell⁵, Catherine A. Clark^{6,7}, Colin Littlefield^{5,8}, Khalid Barkaoui^{9,10,11}, Douglas R. Alves^{12,13}, David R. Anderson^{14,15}, Daniel Bayliss^{14,15}, Francois Bouchy⁴, Edward M. Bryant¹⁶, George Dransfield¹⁷, Elsa Ducrot^{18,19}, Philipp Eigmüller²⁰, Samuel Gill^{14,15}, Edward Gillen^{21,22}, Michaël Gillon⁹, Faith Hawthorn^{14,15}, Matthew J. Hooton³², James A. G. Jackman^{23,14,15}, Emmanuel Jehin²⁴, James S. Jenkins^{25,13}, Alicia Kendall¹, Monika Lendl⁴, James McCormac^{14,15}, Maximiliano Moyano²⁶, Peter Pihlmann Pedersen^{27,32}, Francisco J. Pozuelos²⁸, Gavin Ramsay²⁹, Ramotholo R. Sefako³⁰, Mathilde Timmermans⁹, Amaury H. M. J. Triaud¹⁷, Stephane Udry⁴, Jose I. Vines²⁶, Christopher A. Watson³¹, Richard G. West^{14,15}, Peter J. Wheatley^{14,15}, Sebastián Zúñiga-Fernández⁹

¹ School of Physics and Astronomy, University of Leicester, University Road, Leicester LE1 7RH, UK

² European Space Agency (ESA), European Space Research and Technology Centre (ESTEC), Keplerlaan 1, 2201 AZ Noordwijk, The Netherlands

³ European Southern Observatory, Karl-Schwarzschildstr. 2, D-85748 Garching bei München, Germany

⁴ Département d'astronomie, Université de Genève, 51 chemin Pegasi, 1290 Sauverny, Switzerland

⁵ NASA Ames Research Center, Moffett Field, CA 94035, USA

⁶ Jet Propulsion Laboratory, California Institute of Technology, Pasadena, CA 91109 USA

⁷ NASA Exoplanet Science Institute, IPAC, California Institute of Technology, Pasadena, CA 91125 USA

⁸ Bay Area Environmental Research Institute, Moffett Field, CA 94035, USA

⁹ Astrobiology Research Unit, Université de Liège, Allée du 6 Août 19C, B-4000 Liège, Belgium

¹⁰ Department of Earth, Atmospheric and Planetary Science, Massachusetts Institute of Technology, 77 Massachusetts Avenue, Cambridge, MA 02139, USA

¹¹ Instituto de Astrofísica de Canarias (IAC), Calle Vía Láctea s/n, 38200, La Laguna, Tenerife, Spain

¹² Departamento de Astronomía, Universidad de Chile, Casilla 36-D, Santiago, Chile

¹³ Centro de Astrofísica y Tecnologías Afines (CATA), Casilla 36-D, Santiago, Chile

¹⁴ Centre for Exoplanets and Habitability, University of Warwick, Gibbet Hill Road, Coventry, CV4 7AL, UK

¹⁵ Dept. of Physics, University of Warwick, Gibbet Hill Road, Coventry, CV4 7AL, UK

¹⁶ Mullard Space Science Laboratory, University College London, Holmbury St Mary, Dorking, Surrey, RH5 6NT, UK

¹⁷ School of Physics & Astronomy, University of Birmingham, Edgbaston, Birmingham B15 2TT, UK

¹⁸ Paris Region Fellow, Marie Skłodowska-Curie Action

¹⁹ AIM, CEA, CNRS, Université Paris-Saclay, Université de Paris, F-91191 Gif-sur-Yvette, France

²⁰ Institute of Planetary Research, German Aerospace Center, Rutherfordstrasse 2, 12489 Berlin, Germany

²¹ Astronomy Unit, Queen Mary University of London, Mile End Road, London E1 4NS, UK

²² Astrophysics Group, Cavendish Laboratory, J.J. Thomson Avenue, Cambridge, CB3 0HE, UK

²³ School of Earth and Space Exploration, Arizona State University, Tempe, AZ, 85287, USA

²⁴ STAR Institute, University of Liège, Allée du 6 Août 19c, 4000 Liège, Belgium

²⁵ Núcleo de Astronomía, Facultad de Ingeniería y Ciencias, Universidad Diego Portales, Av. Ejército 441, Santiago, Chile

²⁶ Instituto de Astronomía, Universidad Católica del Norte, Angamos 0610, 1270709, Antofagasta, Chile

²⁷ Department of Physics, ETH Zurich, Wolfgang-Pauli-Strasse 2, CH-8093 Zurich, Switzerland

²⁸ Instituto de Astrofísica de Andalucía (IAA-CSIC), Glorieta de la Astronomía s/n, 18008 Granada, Spain

²⁹ Armagh Observatory & Planetarium, College Hill, Armagh, BT61 9DG, UK

³⁰ South African Astronomical Observatory, P.O Box 9, Observatory 7935, Cape Town, South Africa

³¹ Astrophysics Research Centre, School of Mathematics and Physics, Queen's University Belfast, BT7 1NN Belfast, UK

³² Cavendish Laboratory, JJ Thomson Avenue, Cambridge CB3 0HE, UK

Accepted XXX. Received YYY; in original form ZZZ

ABSTRACT

We report the discovery of a brown dwarf orbiting a M1 host star. We first identified the brown dwarf within the Next Generation Transit Survey data, with supporting observations found in *TESS* sectors 11 and 38. We confirmed the discovery with follow-up photometry from the South African Astronomical Observatory, SPECULOOS-S, and TRAPPIST-S, and radial velocity measurements from HARPS, which allowed us to characterise the system. We find an orbital period of ~ 1.25 d, a mass of $69.0^{+5.3}_{-4.8} M_J$, close to the Hydrogen burning limit, and a radius of $0.95 \pm 0.05 R_J$. We determine the age to be >0.5 Gyr, using model isochrones, which is found to be in agreement with SED fitting within errors. NGTS-28Ab is one of the shortest period systems found within the brown dwarf desert, as well as one of the highest mass brown dwarfs that transits an M dwarf. This makes NGTS-28Ab another important discovery within this scarcely populated region.

Key words: stars:brown dwarfs

1 INTRODUCTION

Brown dwarfs (BDs) are intriguing objects, located between high mass exoplanets and low mass main sequence stars. Their masses are canonically defined to lie in the $13 M_J$ to $80 M_J$ range (Burgasser 2008; Burrows & Liebert 1993; Baraffe et al. 2002; Triaud et al. 2017). BDs never become massive enough to burn hydrogen in their core, supporting themselves through electron degeneracy pressure (Whitworth 2018) although some BDs are massive enough to burn deuterium (Whitworth 2018; Bate et al. 2002). The first BDs were not discovered until 1995 (Gliese 229B: Nakajima et al. 1995; Teide 1: Rebolo et al. 1995) but candidates were found with radial velocity methods previous to this (HD114762: Latham et al. 1989). However, thousands have since been observed with the majority being isolated BDs.

Due to their degenerate nature, BDs exhibit an age-radius-mass-temperature degeneracy: their radii contract over their lifetimes as they cool (Burrows & Liebert 1993). If the radius can be determined, how the BD evolves over their lifetimes can be predicted and therefore can be used as an age estimate (e.g. Marley et al. 2021; Baraffe et al. 2003, 2015). However, most BDs do not have accurately measured radii due to being isolated objects. BDs found in eclipsing binary systems therefore offer an opportunity to directly measure their radii, breaking this degeneracy.

Only two BD-BD eclipsing binary systems are known to date (Stassun et al. 2006; Triaud et al. 2020), and searching for BDs around main sequence stars is an obvious place to look. Fortunately, BD radii are similar to that of Jupiter (Burrows & Liebert 1993) making them as detectable as Jupiter-sized exoplanets in exoplanet surveys (e.g. Acton et al. 2021; Grieves et al. 2021; Carmichael et al. 2021).

However, the radii of BDs can also be affected by exterior factors to the BD, such as interactions with their host star through irradiation (Casewell et al. 2020b). Irradiation will affect the BD atmosphere by heating it, and is also thought to cause a BD's radius to be inflated (e.g. Kelt-1b: Siverd et al. (2012), WD1032+11: Casewell et al. (2020a)) in the same way that is seen for hot Jupiters (e.g. Thorngren et al. 2021; Tilbrook et al. 2021; Alves et al. 2022).

To date, 34 transiting BDs have been discovered orbiting within 3 AU of a main sequence star (e.g. Carmichael et al. 2022 and references therein) which is small compared to the thousands of isolated BDs. This number is also much lower than would be expected when compared to the population of low mass eclipsing binary systems or the hot Jupiter exoplanet population. This local minima between these populations is called the 'brown dwarf desert' (Grether & Lineweaver 2006). The desert is thought to be caused by the differences in formation mechanisms between exoplanets and stars (Grieves et al. 2021; Ma & Ge 2014) but is still not well understood.

Since it was first identified, the BD desert is still scarcely populated, even including recent works using large photometric surveys (see Figure 7 of Triaud et al. 2017). Multiple studies have looked into characteristics of objects within the BD desert. Ma & Ge (2014) discussed whether there is a relationship between mass of the BD and eccentricity. They considered all known exoplanets (at the time), along with all BD candidates around FGK stars (spanning 0-100 M_J) and determined that they could separate BDs at a mass of $42.5 M_J$ into two populations. Those which are more massive ($> 42.5 M_J$) appeared to display a period-eccentricity distribution with a circularisation limit of ~ 12 d, similar to stellar binaries. This is due to objects with shorter periods (up to 12 d) having circular orbits, and those with longer orbits having a flat but wide distribution of eccentricities (as seen in Ma & Ge 2014; Raghavan et al. 2010). The lower mass

population displayed a period-eccentricity trend similar to exoplanets, where higher mass objects (up to the $42.5 M_J$ split) have lower eccentricities. Ma & Ge (2014) determined that these trends point to objects with masses above $42.5 M_J$ forming via stellar formation mechanisms, instead of via protoplanetary discs (Ma & Ge 2014).

Other studies have since sought to find this split population in eccentricity distributions within their observed sample of BDs. Grieves et al. (2021) state that they do not see this trend or evidence of Ma & Ge (2014)'s split population at $42.5 M_J$. Although they note their small sample size as they only include transiting BDs and low mass stars ($12.9 M_J$ to $149.8 M_J$, Grieves et al. 2021) and not high mass exoplanets. Carmichael et al. (2019) also does not find a split at $42.5 M_J$. However, they conclude it is due to there not being a split in the population at all, as opposed to a lack of objects. This illustrates a clear need for more objects to populate this region, to aid in the understanding of whether there is a mass split at $42.5 M_J$ due to formation mechanisms.

Metallicity ([Fe/H]) has also been looked at within the brown dwarf sample. Ma & Ge (2014) did not find any evidence of a split population at $42.5 M_J$ when comparing [Fe/H], and found a mean [Fe/H] of -0.05 . Jenkins et al. (2015) compared the mean [Fe/H] values for BDs, stellar binaries and exoplanets. They found that BDs and stellar binaries have comparable sub-solar mean [Fe/H] values, where as exoplanets have an above solar mean [Fe/H]. The brown dwarfs within the Jenkins et al. (2015) sample were mainly found with radial velocity methods, rather than the transiting sample as is done in this work.

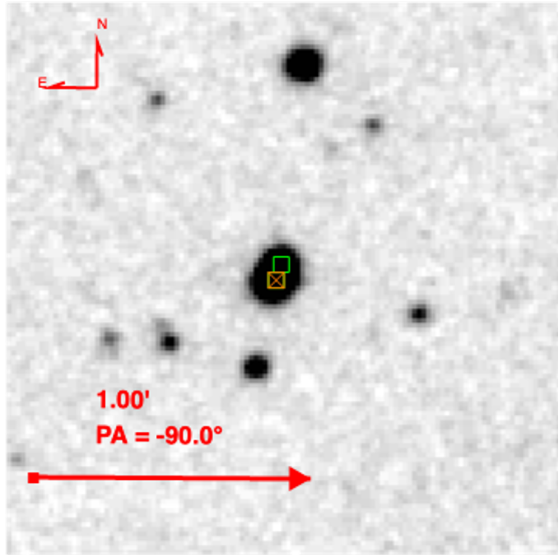
In this paper we present the discovery of NGTS-28Ab, a transiting BD lying within the 'BD desert'. In section 2 we detail the various photometric and spectral observations obtained. In Section 3, the methods used to analyse both the host star and BD are described, along with the probable common proper motion companion, NGTS-28B. Section 4 discusses the importance of this discovery in terms of its position within the BD desert and analyses the eccentricity and age of NGTS-28Ab further.

2 OBSERVATIONS

There is a star located ~ 4 arcseconds from NGTS-28A, meaning the photometry of NGTS-28A was blended with that nearby object, hereafter referred to as NGTS-28B. NGTS-28B is of similar magnitude and is likely a common proper motion companion to NGTS-28A (see Section 3.1). NGTS-28AB refers to the combination of both NGTS-28A and NGTS-28B where both stars are present in a photometric aperture. NGTS-28AB was first observed with the Next Generation Transit Survey, hereafter NGTS (Wheatley et al. 2018) and later the *Transiting Exoplanet Survey Satellite*, TESS (Ricker et al. 2014). Due to NGTS and TESS having pixel sizes of 5 arcsec (Wheatley et al. 2018) and 21 arcsec (Ricker et al. 2014), respectively, the photometry from both these facilities of NGTS-28A was blended with that of NGTS-28B (Figure 1). We obtained follow-up observations in various wavelengths (Table 1) using SHOC on the 1 m Lesedi telescope at the South African Astronomical Observatory (SAAO, Coppejans et al. 2013) to obtain observations that were not blended. We obtained follow up photometry with SPECULOOS-S and TRAPPIST-S, most of which were uncontaminated by NGTS-28B. We obtained six spectra in total with HARPS (Mayor et al. 2003), four of the host star NGTS-28A, and two of NGTS-28B. A summary of these observations can be found in Table 1 and 2.

Table 1. Photometric observations of NGTS-28Ab.

Instrument	Bandpass	Cadence (s)	Number of transits	Observation date
NGTS	520-890 nm	13	26	2017 Jan 2 to 2017 Aug 21
TESS Sector 38	600-1000 nm	120	20	2021 Apr 29 to 2021 May 25
TESS Sector 11	600-1000 nm	1800	16	2019 Apr 22 to 2019 May 21
SAAO	I	10 s	1	2018 July 4
SPECULOOS-S	g', r', i'	147, 52, 26	3	2023 Apr 18
SPECULOOS-S	$z', I + z'$	19, 12	2	2023 June 15
TRAPPIST-S	z'	60	1	2023 Mar 29
TRAPPIST-S	$I + z'$	45	1	2023 Apr 18


Figure 1. DSS image showing NGTS-28A (orange box with cross) and NGTS-28B (green box) blended on sky, along with other nearby objects. North and East are shown on the figure in the top left corner as well as a 1 arcmin position angle (PA) arrow for scale.

2.1 Photometry

2.1.1 NGTS

NGTS-28A was initially observed with NGTS a twelve-telescope array situated at ESO's Paranal Observatory, Chile (Wheatley et al. 2018). The observations taken between the dates 2017 January 2 to 2017 August 21. The twelve, 20 cm telescopes cover almost 100 deg² of sky and operate in a custom bandpass of 520 nm to 890 nm (Wheatley et al. 2018). We observed for a total of 135 nights, during which we obtained 199,319 science images with a 13 s cadence.

The raw images were processed following the method discussed in Wheatley et al. (2018) and the lightcurves were detrended using SysREM (Tamuz et al. 2005). After detrending, transits were detected using a BOXED LEAST SQUARES algorithm. A total of 26 transits were detected, which can be seen in Figure 2 and a phase-fold of the data on the predicted period can be seen in Figure 3. The star is clearly variable, but we determined an orbital period of 1.25 d and a transit depth of around 1.36 per cent.

2.1.2 TESS

TESS obtained 30 minute cadence photometry of NGTS-28AB, observing between 2019 April 22 to 2019 May 21 for sector 11 and

2021 April 29 to 2021 May 25 for sector 38. Sector 38 also had two-minute cadence data. The 30 minute full frame image has a precision around 5 mmag (Ricker et al. 2014). Figure 4 shows the full SPOC lightcurve, along with the a cropped version showing a flare and the individual transits.

The transits within both TESS sectors were independently identified by the TESS team and NGTS-28B was initially named TOI (TESS Object of Interest) 4339 on 2022 September 09. NGTS-28A has since been found to be the true host star. NGTS-28A was named TOI 6110 on 2023 May 27. The two-minute cadence data was processed using the SPOC pipeline (Jenkins et al. 2016). As with the NGTS data, the TESS photometry is blended. TESS provides two flux values: SAP flux and PDCSAP flux. The PDCSAP flux removes systematics in the lightcurve, as well as correcting for dilution. Within the PDCSAP flux, we noticed the transit depths were much larger than expected. PDCSAP flux lightcurve has been corrected for dilution, assuming the transit is on the companion star, NGTS-28B and not NGTS-28A. We therefore chose to use SAP flux instead and modelled the data using a Gaussian process (GP) fit during the global modelling process to remove systematics in the data. We also performed our own dilution calculation to use within the global modelling. The TESS data contains a total of 20 transits in the two-minute cadence data. Unfortunately, the sector 11 30-minute cadence data includes a large (5 d) data gap in the centre of the observation run, despite this it was used to provide confirmation of the ephemeris.

2.1.3 SAAO

We obtained V and I band transit light curves with the SAAO 1.0 m telescope (Table 1) and one of the frame-transfer SHOC (Sutherland High Speed Photometer, (Coppejans et al. 2013)) CCD cameras, specifically "SHOC'n'awe", between 2018 and 2020. On the 1.0 m, the SHOC cameras have a pixel scale of 0.167 arcsecs/pixel. Combined with 4×4 binning, this gave a pixel resolution of 0.67 arcsecs. Both datasets were de-biased and flat-fielded using SAAO's local Python-based SHOC reduction pipeline, which utilises IRAF (Tody 1986, 1993) and PyRAF (Science Software Branch at STScI 2012) tasks.

We used the Starlink package AUTOPHOTOM (Eaton et al. 2014) to perform aperture photometry on both our target and several suitable comparison stars in the $2.85' \times 2.85'$ field of view. Since the two stars NGTS-28A and NGTS-28B lie ≈ 4 arcsecs apart, a 2 pixel radius aperture was chosen, together with a background annulus with radius between 12 and 14 pixels, to try to avoid contaminating light. Even so, while the two stars are indeed fully resolved in the SAAO V band images, they are increasingly blended in the longer wavelength I filter image.

The measured fluxes of the comparison stars were used to perform differential photometry on each of NGTS-28A and NGTS-28B,

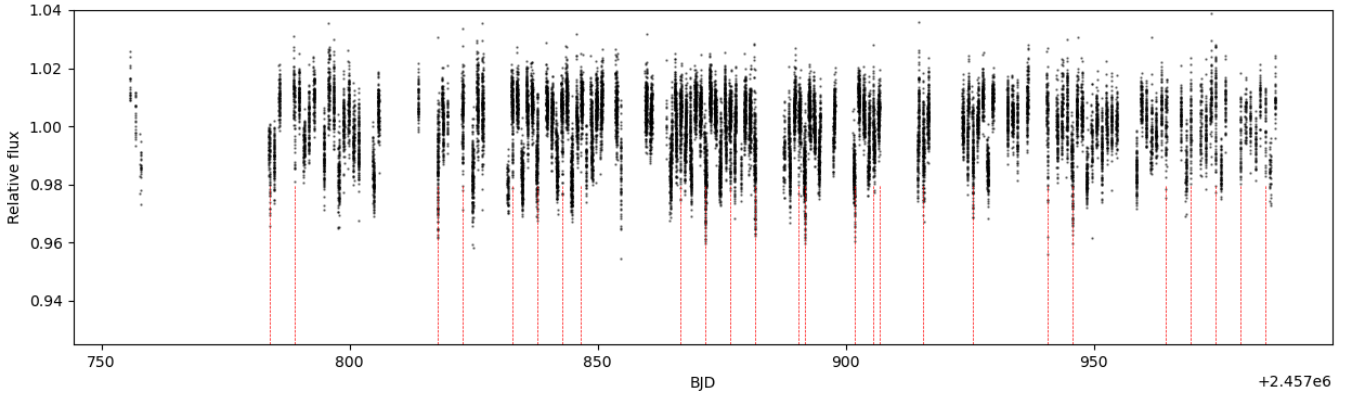


Figure 2. The full NGTS lightcurve for NGTS-28AB with the transit positions marked by the red dashed lines.

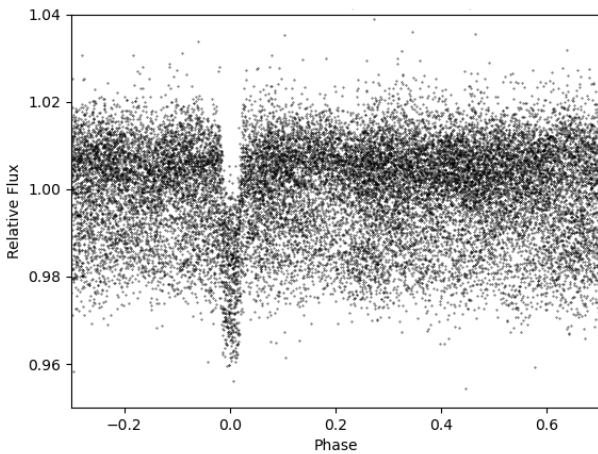


Figure 3. The NGTS lightcurve, phase-folded on the 1.254145 d period from NGTS.

which confirms that the transit is on NGTS-28A. While the transit was detected within the SAAO *V* data, we did not use this in our global modelling. This is due to concerns over the noise levels within the data, with a large amount of scatter seen in the baseline.

2.1.4 SPECULOOS-South

We obtained simultaneous, multi-wavelength observations of NGTS-28A with the three of the four, 1.0-m ‘Search for Planets Eclipsing Ultra-cool Stars’ (SPECULOOS-S) telescopes at Cerro, Paranal (Jehin et al. 2018; Delrez et al. 2018; Sebastian et al. 2021). Each SPECULOOS-S telescope is equipped with a 2K×2K detector with a pixel scale of 0.35 arcsec and an on-sky field of view of 12×12 arcminutes. On 2023 April 18, we simultaneously observed a transit on NGTS-28A in the Sloan-*g'*, *-r'* and *-i'* filters on the Io, Europa and Callisto telescopes, respectively. We also obtained transits in *z'* and *I+z'* filters on 2023 June 15 using the Io and Europa telescopes. Details on the cadence for each observation can be found in Table 1.

We processed all of the data following the PROSE pipeline detailed in Garcia et al. (2022). Briefly, PROSE is a modular and adaptable pipeline, which performs image reduction/calibration, then differential aperture photometry on NGTS-28A. The differential aperture photometry creates a weighted, artificial comparison star from all available objects within the image as described in Broeg et al.

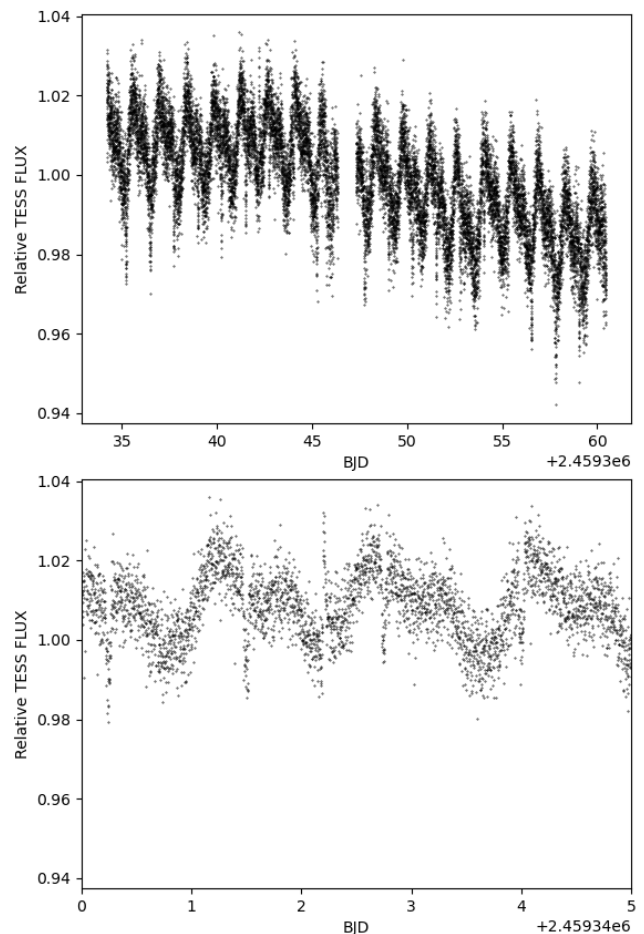
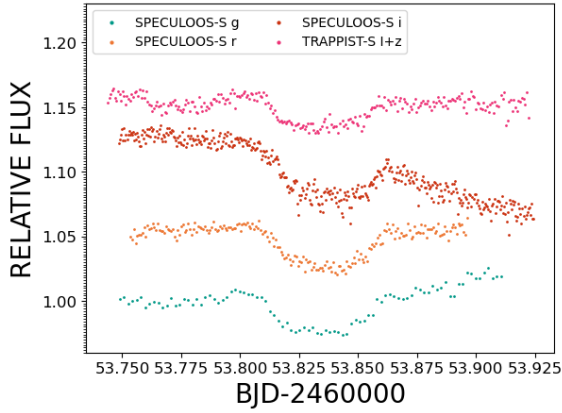


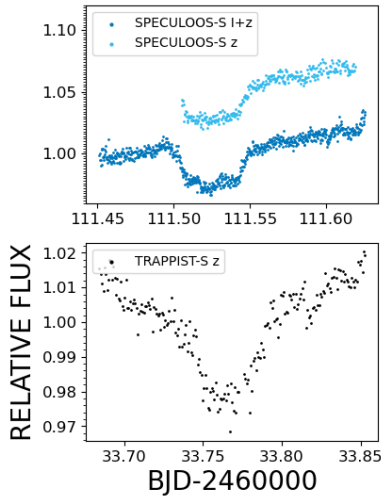
Figure 4. Top: The full TESS lightcurve for NGTS-28AB two-minute cadence data in sector 38, showing the transits. An apparent rotation of the object can also be seen. Bottom: A snippet of the top image, showing the apparent rotation of the object and a flare.

(2005). The lightcurves are then detrended for airmass, full-width half-maximum and sky background, with PROSE, producing the normalised, resultant curves seen in Figure 5. This procedure has been successfully used for previous SPECULOOS-S observations (e.g. Barkaoui et al. 2023; Dransfield et al. 2024).

After performing aperture photometry, we confirmed all the



(a)



(b)

Figure 5. Normalised lightcurves of the new data from SPECULOOS-S and TRAPPIST-S. Offsets have been applied to some of the fluxes for clarity.

SPECULOOS-S transits, except for the i' filter observation, were uncontaminated. Due to high background in the g' and r' observations, the last few points of each were discarded from global modelling.

2.1.5 TRAPPIST

The TRANSiting Planets and PlanetIsms Small Telescope (TRAPPIST-S, Gillon et al. 2011; Jehin et al. 2011) is a 0.6 m robotic telescope based at ESO’s La Silla Observatory. TRAPPIST-S is equipped with a 2K×2K detector with a 0.6 arcsec pixel scale, and a field of view of 22 × 22 arcminutes. Two single-transit observations were taken at TRAPPIST-S. The z' filter observation was made on 2023 March 29, and the $I + z'$ filter observation was made on 2023 April 18. Cadence for each observation can be seen in Table 1. The PROSE pipeline (Garcia et al. 2022) was also used for the TRAPPIST-S data reduction, as in Section 2.1.4. The resultant, relative flux lightcurves can be seen in Figure 5.

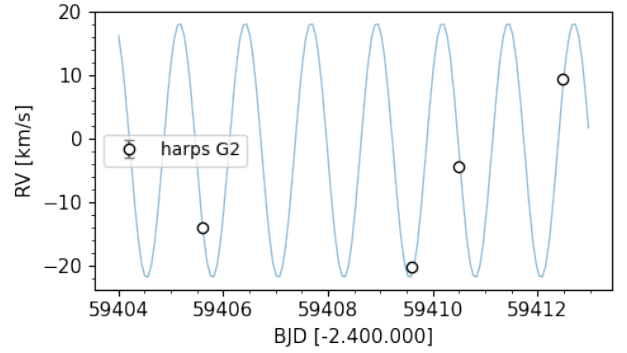


Figure 6. HARPS time series plot of the radial velocity points from the spectra, with a G2 mask used.

2.2 Radial Velocities

2.2.1 HARPS

We obtained high resolution spectra of both NGTS-28A and NGTS-28B using HARPS, an echelle spectrograph on ESO’s 3.6 m telescope at La Silla Observatory (Mayor et al. 2003). HARPS is fibre-fed with an on-sky diameter of 1 or 1.4 arcsec (Mayor et al. 2003). There is also the option of a second fibre simultaneously monitoring the sky or wavelength solution of the instrument. It covers a spectral range of 380 to 690 nm, has a resolution of $R = 115000$ (Mayor et al. 2003).

For our observations we used the default high accuracy mode with a 1 arcsec science fibre and fibre B on sky (for more information see: Mayor et al. 2003). We used exposures of 2400 s for each spectrum, except for the final exposure for NGTS-28A which has an exposure time of 1800 s. The spectra had signal-to-noise ratios that ranged between 3.4 and 4.7, and was extracted per pixel in order 50 (corresponding to ~ 550 nm). We obtained four spectra of NGTS-28A between 2021 July 10 - 2021 July 16 (Table 2). On 2021 June 11 - 2021 June 12, we also obtained two spectra of NGTS-28B. The mean RV precision reached with the four NGTS-28A observations was 0.0515 km s^{-1} .

The data were reduced using the HARPS pipeline and radial velocities (RVs) measured using a G2V mask and the cross-correlation technique (Pepe et al. 2002; Baranne et al. 1996). A G2V mask was used as it has been highly optimised for RV measurements but also because the spectra have low signal-to-noise (meaning only the strongest lines are detected). In addition, NGTS-28A is rotating fast, meaning many lines are blended. Figure 6 shows the time series for the NGTS-28A radial velocity measurements.

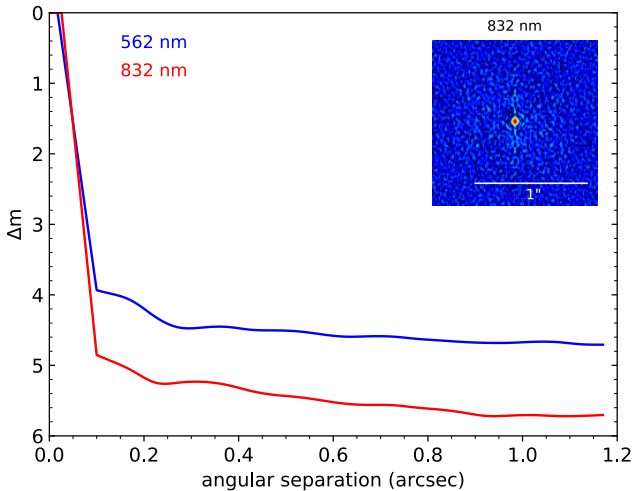
The pipeline also produces values for the bisector inverse slope (BIS, Dall et al. 2006; Queloz et al. 2001) which can be an indicator for variability or a blended eclipsing binary (Günther et al. 2018; Santos et al. 2002). The automatic pipeline calculation of the BIS picked up a local minima in the cross-correlation function (CCF) and computed BIS values from that. To mitigate this, we binned the CCF to 5 km s^{-1} in velocity space and re-calculated the BIS. The radial velocity values for NGTS-28B and BIS values for both objects are also in Table 2.

2.3 High-resolution imaging with ZORRO

Nearby companion stars can appear to mimic transit signatures in lightcurves, as well as affecting the detected depth of any real transiting event meaning the derived radii of any secondary object will

Table 2. Radial velocity measurements of NGTS-28A and NGTS-28B and the associated uncertainties and BIS values from HARPS.

BJD	Radial velocity [km s ⁻¹]	BIS [km s ⁻¹]
NGTS-28A		
2459405.599495	-13.99 ± 0.049	-0.34 ± 0.10
2459409.590870	-20.22 ± 0.055	1.08 ± 0.11
2459410.492873	-4.38 ± 0.053	2.87 ± 0.11
2459412.475762	9.46 ± 0.049	0.37 ± 0.10
NGTS-28B		
2459376.625674	-2.01 ± 0.048	0.06 ± 0.10
2459377.543570	-1.75 ± 0.049	0.76 ± 0.10

**Figure 7.** 5- σ contrast curves for speckle imaging in both 562 nm and 832 nm filters. This is plotted as a function of the angular separation from 0.02 to 1.2 arcsec. The reconstructed image for 832 nm can be seen in the top right of the figure. No close companions have been found within these limits.

be incorrect (Howell et al. 2011; Furlan & Howell 2017). High resolution imaging of the host star is one way to determine if the host star is actually an unresolved binary.

We performed speckle imaging with ZORRO on 2023 May 08 (Howell & Furlan 2022; Scott et al. 2021). The resultant 5- σ contrast curve can be seen in Figure 7, where the two filters used (562 nm and 832 nm, blue and red respectively) are plotted. We obtained 12 sets of 1000 images with an exposure time of 0.06 seconds, which was processed using the standard pipeline, detailed in Howell et al. (2011).

Figure 7 shows no nearby stellar companions detected near NGTS-28A to within the contrast (4 magnitudes at 562 nm and 5.8 magnitudes at 832 nm) and the angular separation (0.02-1.2 arcsec) limits of the observation. Meaning we detected no stellar companion between around 2.5 and 147.9 AU around NGTS-28A. A reconstructed 832 nm image can be seen in the inset of Figure 7.

3 ANALYSIS

3.1 NGTS-28B

Figure 1 shows the DSS image of NGTS-28Ab and shows NGTS-28A is blended with another star (NGTS-28B), with an on sky separation of ~ 3.6 arcsec. We compared the *Gaia* DR3 kinematics (Gaia Collaboration et al. 2016, 2022) for NGTS-28B and NGTS-28A (Table 3). NGTS-28B has a proper motion and parallax in *Gaia* DR3 that is

similar to that of NGTS-28A although the proper motion is not consistent within the errors. However, Mugrauer et al. (2023) have found NGTS-28A and NGTS-28B to be co-moving within their multiplicity study. Combining the distance to NGTS-28A and angular separation (3.6 arcsec) of NGTS-28AB, the separation is ~ 443 AU. This wide separation also means NGTS-28B will not have any substantial gravitational effect on NGTS-28A, and so will not affect orbital radial velocity measurements for NGTS-28Ab over the time span of the observations taken.

Within 15 arcsec, there is a third object which has a *Gaia* *G* magnitude of 20.3 (Gaia Collaboration et al. 2022), but it does not have a parallax or proper motion which is consistent with being a common proper motion companion. This object is too faint to have a significant affect on our photometry. We also searched the wider field within 5' for proper motion companions, but none were found. Within 60 arcseconds, there are 18 objects, but none of which are brighter than the host star. It is unlikely any of these objects have a significant contribution to the photometry of the system due to their separation, especially compared to NGTS-28B. NGTS-28B has been taken into consideration within our analysis, as blending within the aperture will affect the depth of the measured transit (Ciardi et al. 2015). This is discussed further in Section 3.3.1.

3.2 NGTS-28A: Host star parameters

We analysed NGTS-28A using spectral fitting and spectral energy distribution (SED) fitting. Table 3 gives the proper motion, parallax and magnitudes from *Gaia* DR3 (Gaia Collaboration et al. 2016, 2022), *TESS*, 2MASS (Skrutskie et al. 2006), and PanSTARRS (Chambers et al. 2016; Flewelling et al. 2020).

3.2.1 Spectral analysis

We analysed the HARPS spectra with SPECMATCH-EMP (Yee et al. 2017) for both NGTS-28A and NGTS-28B. First, we shifted the spectra into the rest frame to remove the radial velocity variations, then co-added the spectra to obtain a single spectrum with a higher signal-to-noise ratio than the individual spectra, although the total signal-to-noise ratio (SNR) of the co-added spectrum of NGTS-28A was still low per pixel (5.5). We then used SPECMATCH-EMP to compare our spectra to the KECK/HIRES libraries of template spectra in order to select a few 'best fitting' objects to the target spectra. Linearly combined spectra of the comparison objects were then created and compared to the target spectra, to get a best fit. The output parameters are calculated using the weighted averages of the linearly combined spectra. SPECMATCH-EMP then uses χ^2 statistics to test how good of a fit the estimated parameters are to the data.

We determined that NGTS-28A has a mass of $0.56 \pm 0.08 M_{\odot}$, radius of $0.53 \pm 0.1 R_{\odot}$ and a T_{eff} of 3630 ± 70 K. We also found it has a $\log g$ of 4.74 ± 0.12 and a $[\text{Fe}/\text{H}]$ of 0.36 ± 0.09 . For NGTS-28B we determined a mass of $0.39 \pm 0.08 M_{\odot}$ radius of $0.39 \pm 0.1 R_{\odot}$ and a T_{eff} of 3500 ± 70 K. We also found a $\log g$ of 4.87 ± 0.12 and a $[\text{Fe}/\text{H}]$ of 0.00 ± 0.09 . The errors estimated by SPECMATCH-EMP are likely underestimates due to the low signal-to-noise ratio of the spectra, which is not considered within SPECMATCH-EMP. The SPECMATCH-EMP code uses fixed errors for all results, which depend only on the property's value. For example, the T_{eff} will have an adopted error of 70 K if it is less than 4500 K and an adopted error of 110 K if T_{eff} is greater than or equal to 5500 K. For more information we refer the reader to the software paper, Yee et al. (2017).

The two objects are of a similar T_{eff} with NGTS-28B being slightly

Table 3. Magnitudes, parameters and kinematics of NGTS-28A and NGTS-28B. The kinematics of the two objects are from *Gaia* DR3 and the photometry is from *Gaia* DR3 (Gaia Collaboration et al. 2022), 2MASS (Skrutskie et al. 2006), PanSTARRS (Chambers et al. 2016; Flewelling et al. 2020). The *TESS* magnitude is from ExoFOP (Ricker et al. 2014). We list parameters of NGTS-28A and NGTS-28B found using SPECMATCH-EMP as priors for ARIADNE. Due to the low SNR of the spectra and the blending in photometry available, the errors in the parameters are likely underestimated and represent numerical errors.

Parameter	NGTS-28A	NGTS-28B
<i>Gaia</i> Source ID	6172969891098581120	6172969891098581248
RA	14:11:43.0	14:11:42.9
Dec	-29:58:28.39	-29:58:26.32
pmRA [mas yr ⁻¹]	-78.61 ± 0.02	-79.06 ± 0.04
pmDec [mas yr ⁻¹]	24.74 ± 0.02	23.77 ± 0.03
Parallax [mas]	8.113 ± 0.020	8.085 ± 0.034
Distance [pc]	123.25 ± 0.31	123.86 ± 0.53
Magnitudes		
<i>Gaia</i> G	14.137 ± 0.001	15.249 ± 0.001
<i>Gaia</i> BP	15.250 ± 0.006	16.550 ± 0.005
<i>Gaia</i> RP	13.088 ± 0.003	14.097 ± 0.002
<i>TESS</i> [T]	13.074 ± 0.009	14.064 ± 0.008
2MASS _J	11.664 ± 0.039	12.552 ± 0.025
2MASS _H	11.057 ± 0.047	11.958 ± 0.038
2MASS _{K_s}	10.832 ± 0.037	11.757 ± 0.027
PanSTARRS _g	15.623 ± 0.004	16.923 ± 0.007
PanSTARRS _r	14.373 ± 0.003	15.716 ± 0.010
PanSTARRS _i	n/a	14.568 ± 0.006
Fitted Parameters		
T _{eff} (K)	3626 ⁺⁴⁷ ₋₄₄	3441 ⁺⁷⁰ ₋₅₂
log g (dex)	4.74 ^{+0.10} _{-0.09}	4.85 ^{+0.13} _{-0.14}
[Fe/H] (dex)	-0.14 ^{+0.16} _{-0.17}	-0.02 ^{+0.26} _{-0.23}
M _A [M _⊙]	0.56 ^{+0.02} _{-0.02}	0.43 ^{+0.01} _{-0.02}
R _A [R _⊙]	0.59 ^{+0.03} _{-0.03}	0.42 ^{+0.03} _{-0.03}
Age [Gyr]	6.99 ^{+3.09} _{-6.49}	2.06 ^{+10.08} _{-1.49}

cooler than NGTS-28A. We also find that NGTS-28B is less massive with a smaller radius than NGTS-28A. These values are consistent with NGTS-28B being fainter than NGTS-28A. The age of both objects are also found to be in agreement within errors, supporting that they are likely common proper motion companions. We used the log g, radius and T_{eff} of NGTS-28A and NGTS-28B as priors for ARIADNE.

3.2.2 SED fitting

We fit the broadband photometry in Table 3 for NGTS-28A and NGTS-28B using ARIADNE, a SED fitting tool (Vines & Jenkins 2022) which uses six atmospheric models (PHOENIX: Husser et al. (2013), BT-SETTL: Allard et al. 2012, BT-NEXTGEN: Allard et al. 2012; Hauschildt et al. 1999, BT-COND: Allard et al. 2012, CASTELLI & KURUCZ: Castelli & Kurucz 2004, KURUCZ: Kurucz 1993) to determine various stellar parameters.

For NGTS-28A and NGTS-28B we used T_{eff}, radius and log g from SPECMATCH-EMP as priors for the ARIADNE fit. This produced the values in Table 3. It is likely that these values have slightly underestimated errors due to how blended NGTS-28A and NGTS-28B are in the optical photometry.

The SED for NGTS-28A is shown in Figure 8 with the PHOENIX v2 model spectra. Synthetic photometry points, and the residuals

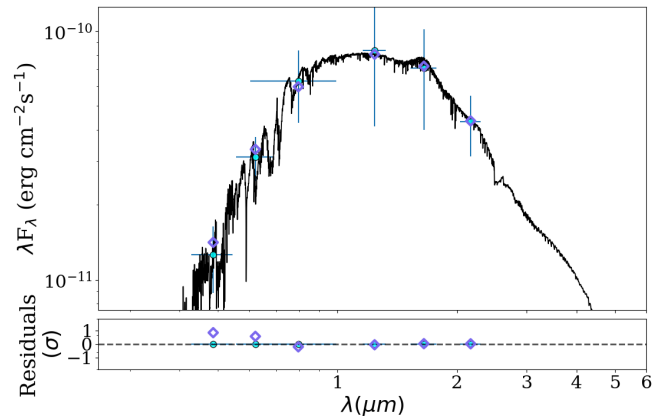


Figure 8. SED fit produced by ARIADNE. Black line shows the PHOENIX V2 model, light blue points show the various catalogue photometry points for NGTS-28A and the purple diamonds show the synthetic photometry fit. Plotted underneath are the residuals for the data and synthetic photometry.

between the synthetic and real photometry points are also seen in Figure 8. The data in Table 3 were taken from the Bayesian Model Average output from ARIADNE.

The ages from ARIADNE are in agreement with each other but the errors very large. The mass and radius of NGTS-28B are smaller than NGTS-28A, as expected when compared to SPECMATCH-EMP.

To obtain rough estimates for the spectral types of both NGTS-28A and NGTS-28B the T_{eff} values were compared to Figure 5 of Rajpurohit et al. (2013). In Rajpurohit et al. (2013)'s figure, the T_{eff} values are plotted with spectral type to show a trend of how T_{eff} values change as you progress to later M dwarf types, along with multiple atmospheric models for comparison. Using the T_{eff} values for NGTS-28A and NGTS-28B, we compared to this figure (Rajpurohit et al. 2013) to estimate a spectral type for both objects. We estimate a spectral type of ~M1 for NGTS-28A and ~M2 for NGTS-28B. We compared this to the Mamajek spectral types (Pecaut & Mamajek 2013) which were estimated with ARIADNE. ARIADNE estimates a M1.5 and M3 spectral classification for NGTS-28A and NGTS-28B, respectively. Comparing the results from both these methods provides a good estimate for the spectral type of both stars. Although more detailed methods can be used, they are not necessary for understanding NGTS-28Ab, and are limited by the low signal-to-noise spectra that are available.

3.3 NGTS-28Ab Parameters

Due to the complexity of the system, NGTS-28Ab's parameters involved a multi-step process to get the most accurate results possible. NGTS-28Ab was analysed using ALLESFITTER (Günther & Daylan 2019, 2021). ALLESFITTER is a statistical tool used to fit lightcurve and radial velocity data to produce estimations for parameters of the system (Günther & Daylan 2019, 2021). It utilises MCMC and dynamic nested sampling (DNS) methods to estimate the best fitting parameters to the data, which can simultaneously be provided from multiple instruments and bandpasses, making use of various software including models such as ELLC (Maxted 2016) and samplers such as DYNesty (Speagle 2020) and EMCEE (Foreman-Mackey et al. 2013).

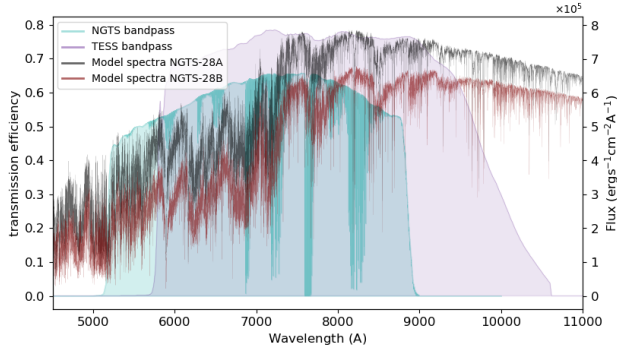


Figure 9. The NGTS bandpass (blue) and *TESS* bandpass (indigo) with NGTS-28A (black) and NGTS-28B (red) model spectra plotted. The NGTS bandpass curve is the product of the quantum efficiency curve of the CCD, the filter transmission curve and an atmospheric absorption curve (Wheatley et al. 2018; Günther et al. 2018). The *TESS* bandpass curve is the product of the filter transmission curve and detector quantum efficiency curve (Ricker et al. 2014).

3.3.1 Estimating Dilution Values

The first step involved calculating estimates for the dilution values for each instrument. We do this in a similar manner to Günther et al. (2018). To do this, we used `PYSYNPHOT` (STScI Development Team 2013). We first obtained the bandpass response function for NGTS and *TESS* (NGTS: Günther et al. 2018; Wheatley et al. 2018, *TESS*: Ricker et al. (2014)). We then obtained model spectra for both NGTS-28A and NGTS-28B using the `PHOENIX` models (Husser et al. 2013) within `PYSYNPHOT`. We randomly sampled 10000 T_{eff} values between the errors of each object’s T_{eff} which created 10000 possible spectra for each object.

The bandpass functions for each instrument and an example model spectra for each object produced by the `PHOENIX` models are plotted in Figure 9. Once we had obtained these, we interpolated the bandpass and spectra, multiplied the stellar spectra by the transmission curve and then integrated over the entire region. This provided flux values for NGTS-28A and NGTS-28B which could be used in equations (1) and (2) from Günther et al. (2018) to calculate the dilution for NGTS-28A. D_B and D_A are the dilution values for NGTS-28B and NGTS-28A, respectively. F_B and F_A are the flux values for NGTS-28B and NGTS-28A, respectively.

$$D_B = 1 - \frac{F_B}{F_A + F_B} \quad (1)$$

$$D_A = 1 - D_B \quad (2)$$

The dilutions were calculated for each of the 10000 spectra, and a mean was calculated. To estimate the error on this value we also calculated a standard deviation for the sample. From this we determined that NGTS-28A has a dilution value of 0.4364 ± 0.0186 and 0.4466 ± 0.0156 in NGTS and *TESS*, respectively. *TESS* PDCSAP estimated a dilution of 0.73 which is larger than the modelled dilution for NGTS-28A or NGTS-28B. This confirmed that the PDCSAP flux has likely been over corrected for this object.

3.3.2 Global Modelling

For the global modelling of the system we modelled the *TESS* two-minute cadence data, the NGTS data which we binned to two-

Table 4. Estimate Matern-3/2 baseline parameters from ALLESFITTER. These were used as priors within the final fit.

Parameter	NGTS	<i>TESS</i>
$\ln \sigma$	$-4.6161^{+0.0587}_{-0.0587}$	$-4.4589^{+0.1135}_{-0.1135}$
$\ln \rho$	$-1.4840^{+0.0764}_{-0.0764}$	$-0.9483^{+0.1049}_{-0.1049}$

minutes, the SAAO, SPECULOOS-S and TRAPPIST-S datasets and the HARPS radial velocity data simultaneously using ALLESFITTER. We removed some data in the SAAO *I* band data due to variable seeing but kept in as much as possible. We also remove some data from the SPECULOOS-S *g'* and *r'* due to high background noise.

We estimated the baseline parameters $\ln \sigma$ and $\ln \rho$ for NGTS and *TESS*, which describe a Gaussian process (GP) baseline with a Matern-3/2 kernel, as seen in Günther & Daylan (2021), using the ‘out of transit’ data in the lightcurve. These were used as priors for the final fit on the in-transit data, varying normally with their errors. HARPS was fit with a hybrid offset and the rest of the photometric datasets were fit with hybrid splines.

For the dynamic nested sampling (`DNS`) fitting, we fixed the dilution for SPECULOOS-S *I* + *z'*, *g'*, *r'* and *z'* to 0 due to there not being any contamination within the aperture. We used the dilution values for NGTS and *TESS* for NGTS-28A from Section 3.3.1 as priors for the fit, and allowed them to vary normally within their errors. For all other datasets we used an initial prior of 0 and allowed it to vary uniformly between 0 and 1. We did not calculate dilution values due to the method of photometry described in Sections 2.1.3, 2.1.4 and 2.1.5.

The limb darkening values for *TESS*, NGTS and all SPECULOOS-S and TRAPPIST-S data were calculated using `LDTK` (Parviainen & Aigrain 2015; Husser et al. 2013) using the Kipping (2013) limb darkening relations. These were fitted with a normal distribution around the priors within the errors produced by `LDTK`. For SAAO *I* data, the limb darkening constants had initial priors of 0.5, varying uniformly between 0 and 1.

All priors, their parameter spaces and resultant values can be seen in Table 5. The epoch is given a prior value and parameter space but is allowed to shift in order to prevent biasing towards one dataset which would cause correlations between epoch and period. We used 500 live points and a tolerance of 0.001. We fit the data with a 0.4 phase width around the transit.

The derived parameters in Table 6. The corner plot for the derived values from this fit are also in the appendix in Figure A1. Plots showing the model fits to the various sources of data can be seen in Figures 10 and 11.

The radius of NGTS-28Ab was therefore found to be $0.95 \pm 0.05 R_J$, with a mass of $69.0^{+5.3}_{-4.8} M_J$. These clearly put NGTS-28Ab within the brown dwarf regime. The derived eccentricity is $0.0404^{+0.0067}_{-0.0101}$, meaning the orbit is close to circular, but still has some eccentricity.

In order to test if the eccentricity is significant, we repeated the model fit with the eccentricity parameters ($\sqrt{e_b} \cos \omega_b$ and $\sqrt{e_b} \sin \omega_b$) fixed to 0, which fixes the eccentricity of the system to 0. We kept all other priors and parameter spaces the same.

Using the Bayesian evidence calculated during the `DNS` fit for both the eccentric and circular model, we calculate a logarithmic Bayes factor of 4.5. Using the criteria from Jeffreys (1998) and Kass & Raftery (1995), this means there is strong evidence for the eccentricity to be a significant measurement, but not definitive. However, due to the Bayes factor being close to the limit of decisive (greater than 4.6), and the fact there is still strong evidence for some level

of eccentricity, we assume the eccentric model to be the most likely. We perform other tests within Section 4.3 of this paper.

4 DISCUSSION

4.1 Population Comparisons: Bridging The Gap

NGTS-28Ab has a mass of $69.0^{+5.3}_{-4.8} M_J$ and a radius of $0.95 \pm 0.05 R_J$, putting it at the upper boundary of the brown dwarf regime. The small radius also suggests that it is a brown dwarf, as most M-dwarfs are predicted by model isochrones to have radii above this value, although there is often a large scatter in the radii of late M-dwarfs (e.g. Parsons et al. 2018). Figure 12, shows the mass-radius plot for known transiting objects within 12-150 M_J , along with the Baraffe et al. 2003, 2015 isochrones for 0.1, 0.5, 1, 5 and 10 Gyr ages. Objects plotted within Figure 12 are shown in Table A1. Figure 12 and Table A1 have been adapted and updated from Grieves et al. (2021). RIK 72B (David et al. 2019) and 2MASS J05352184–0546085 (Stassun et al. 2006) are not included within this distribution due to their youth and hence large radii.

Figure 12 shows NGTS-28Ab (plotted as the black triangle) clearly lies within the brown dwarf regime, with a system mass ratio of $0.1181^{+0.0069}_{-0.0077}$. Bowler et al. (2020) discuss the population statistics of brown dwarfs and hot Jupiters, splitting them based on mass and mass ratio. They found that high mass ratios (greater than 0.01) are more likely to have high eccentricities and indicate stellar formation mechanisms (Bowler et al. 2020). The high mass ratio of this system would make NGTS-28Ab more likely to have formed via stellar formation mechanisms.

NGTS-28Ab sits between the 0.5 and 1 Gyr isochrones on Figure 12. Although this is in agreement with the ages from SED modelling of NGTS-28A and NGTS-28B within errors, the large range of ages estimated for the system indicate it has a likely age range of >0.5 Gyrs.

Low mass M dwarfs have a wide distribution of radii at the low mass end with Parsons et al. (2018) determining that only 25 per cent of the M dwarfs they observed had radii consistent with models, while 12 per cent were inflated. It is not yet known whether this scatter continues into the brown dwarf regime, although the recent discovery of high mass inflated brown dwarfs indicates it may very well do (e.g. Acton et al. 2021; Casewell et al. 2020b; Schaffner et al. 2021).

We determined the metallicity of NGTS-28A using SPECMATCH-EMP and ARIADNE, determining a value of $[Fe/H] = -0.14^{+0.16}_{-0.17}$. Figure A2 shows the mass and metallicity of the known late M dwarf and brown dwarf systems in Table A1. NGTS-28Ab is not an outlier in metallicity within the population for brown dwarfs and low mass stars.

Using ARIADNE, we determined an effective temperatures of 3626^{+47}_{-44} K for NGTS-28A and 3441^{+70}_{-52} K for NGTS-28B. NGTS-28B has a lower temperature than NGTS-28A and it is a redder object. Both objects have early M spectral types. Figure A3 shows the distribution of objects from Table A1 based on effective temperature. It also shows there is a lack of closely transiting objects around K dwarfs, with NGTS-28A as one of the hottest M Dwarf hosts to transiting BDs, lying close to this gap. A similar gap is seen with eclipsing binaries, where tidal forces cause the companions of K-type stars to spiral inward, as discussed in Chaturvedi et al. (2018).

4.2 Rotation and Age

As stated, Figure 12 shows NGTS-28Ab has mass and radius values which are consistent with the 0.5-1 Gyr isochrone from Baraffe et al. 2003, 2015. This is also consistent with the age estimates of NGTS-28A from ARIADNE. A range of ages is not unexpected due to the difficulty in determining ages of low mass stars. Other checks we performed to test the age of the system are discussed in this section.

We performed a check to confirm whether NGTS-28A and NGTS-28B are part of a known young cluster or association. The BANYAN Σ online tool (Gagné et al. 2018) was used. BANYAN Σ uses RA, dec, proper motions and parallax to calculate cluster membership probabilities for various young clusters (up to 800 Myrs) within 150 pc, as well as the probability of the object being field age (~ 5 Gyr). For both stars, BANYAN Σ estimates a 99.9 per cent probability of their being field objects, and are therefore unlikely to be members of young clusters. This high probability of both NGTS-28A and NGTS-28B being field age is consistent with the estimates from ARIADNE.

Another check for youth is whether NGTS-28Ab is in spin-orbit synchronisation with NGTS-28A. Spin-orbit synchronisation is expected for an object of this orbital radius/period. Figure 4 shows the full TESS data for NGTS-28AB in the top panel. From the bottom of Figure 4, an apparent signature due to rotation can be seen, along with the transits and a flare. If it is believed to be the rotation of NGTS-28A alone, it appears the rotation period of the object is very close to, but not quite equal to, the orbital period of NGTS-28Ab. However, it is likely that the lightcurve modulation shows a composite effect of both NGTS-28A and NGTS-28B.

From the large uncertainties in the ages and the high probability of the objects being field age, it is likely that NGTS-28Ab is old. If we make the assumption that the modulation seen in the TESS and NGTS data is from NGTS-28A alone, we can calculate the rotation period using a Lomb-Scargle (LS) periodogram (Lomb 1976; Scargle 1982). We used ASTROPY'S LOMBSCARGLE package (ASTROPY: Astropy Collaboration et al. 2013, 2018, 2022), using a period range between 0.9 and 2 d. The errors associated with the period were calculated by randomly sampling the time-flux array for TESS and NGTS, allowing for duplication of values, and repeating the LS process for each random sample, known as 'bootstrapping'. We repeated the process 1000 times and the standard deviation of the resultant periods was used as the error on the period. We determined the rotation period to be 1.42 ± 0.02 d from the TESS data and 1.42 ± 0.11 d from the NGTS data. Unfortunately, due to the high level of blending in the photometry from TESS and NGTS, we are unable to conclusively say if this rotation period of NGTS-28A is accurate or is a modulation effect caused by the blended NGTS-28B. This uncertainty means we cannot use this rotation period for gyrochronology or to determine any level of spin-orbit synchronisation accurately. Therefore, the mass-radius relation and ARIADNE is used to provide a best estimate for the age of NGTS-28Ab of >0.5 Gyrs.

4.3 System Eccentricity and Tidal Effects

The eccentricity of NGTS-28Ab is $0.0404^{+0.0067}_{-0.0101}$. To test if the eccentricity is a significant detection, we use the method from Lucy & Sweeney (1971), where the detected eccentricity is only significant if the eccentricity value is $2.45\sigma_e$ above the errors:

$$e = \hat{e}, \text{ if } \hat{e} > 2.45\sigma_e, \quad (3)$$

$$e = 0, \text{ if } \hat{e} \leq 2.45\sigma_e, \quad (4)$$

Table 5. The fitted parameters for NGTS-28Ab, produced by ALLESFITTER.

parameter	symbol	prior, parameter space	value
Fitted parameters			
Limb Darkening Parameters			
NGTS LDC 1	$q_{1:NGTS}$	$0.4544, \mathcal{N}(0.4544, 0.0088)$	$0.4517^{+0.0074}_{-0.0078}$
NGTS LDC 2	$q_{2:NGTS}$	$0.2901, \mathcal{N}(0.2901, 0.0022)$	$0.2900^{+0.0018}_{-0.0019}$
TESS Sector 38 LDC 1	$q_{1:TESS}$	$0.3379, \mathcal{N}(0.3379, 0.0054)$	$0.3383^{+0.0046}_{-0.0043}$
TESS Sector 38 LDC 2	$q_{2:TESS}$	$0.2640, \mathcal{N}(0.2640, 0.0019)$	$0.2638^{+0.0017}_{-0.0017}$
SPECULOOS-S I+z' band LDC 1	$q_{1:SPEC_{i,zp}}$	$0.2284, \mathcal{N}(0.2284, 0.0037)$	$0.2290^{+0.0032}_{-0.0033}$
SPECULOOS-S I+z' band LDC 2	$q_{2:SPEC_{i,zp}}$	$0.2199, \mathcal{N}(0.2199, 0.0020)$	$0.2195^{+0.0016}_{-0.0017}$
SPECULOOS-S z' band LDC 1	$q_{1:SPEC_{z,p}}$	$0.2015, \mathcal{N}(0.2015, 0.0031)$	$0.2015^{+0.0026}_{-0.0026}$
SPECULOOS-S z' band LDC 2	$q_{2:SPEC_{z,p}}$	$0.2027, \mathcal{N}(0.2027, 0.0019)$	$0.2030^{+0.0016}_{-0.0017}$
SPECULOOS-S g' band LDC 1	$q_{1:SPEC_{g,p}}$	$0.8945, \mathcal{N}(0.8945, 0.0143)$	$0.8911^{+0.0118}_{-0.0118}$
SPECULOOS-S g' band LDC 2	$q_{2:SPEC_{g,p}}$	$0.3271, \mathcal{N}(0.3271, 0.0016)$	$0.3270^{+0.0014}_{-0.0014}$
SPECULOOS-S i' band LDC 1	$q_{1:SPEC_{i,p}}$	$0.3531, \mathcal{N}(0.3531, 0.0070)$	$0.3550^{+0.0039}_{-0.0039}$
SPECULOOS-S i' band LDC 2	$q_{2:SPEC_{i,p}}$	$0.2678, \mathcal{N}(0.2678, 0.0024)$	$0.2676^{+0.0020}_{-0.0019}$
SPECULOOS-S r' band LDC 1	$q_{1:SPEC_{r,p}}$	$0.7794, \mathcal{N}(0.7794, 0.0151)$	$0.7790^{+0.0127}_{-0.0129}$
SPECULOOS-S r' band LDC 2	$q_{2:SPEC_{r,p}}$	$0.3161, \mathcal{N}(0.3161, 0.0020)$	$0.3162^{+0.0018}_{-0.0018}$
TRAPPIST-S I+z' band LDC 1	$q_{1:TRAP_{i,zp}}$	$0.2284, \mathcal{N}(0.2284, 0.0074)$	$0.2293^{+0.0062}_{-0.0062}$
TRAPPIST-S I+z' band LDC 2	$q_{2:TRAP_{i,zp}}$	$0.2199, \mathcal{N}(0.2199, 0.0040)$	$0.2199^{+0.0034}_{-0.0034}$
TRAPPIST-S z' band LDC 1	$q_{1:TRAP_{z,p}}$	$0.2015, \mathcal{N}(0.2015, 0.0062)$	$0.2020^{+0.0054}_{-0.0054}$
TRAPPIST-S z' band LDC 2	$q_{2:TRAP_{z,p}}$	$0.2027, \mathcal{N}(0.2027, 0.0038)$	$0.2030^{+0.0032}_{-0.0032}$
SAAO I band LDC 1	$q_{1:SAAO_i}$	$0.5, \mathcal{U}(0.0, 1.0)$	$0.2191^{+0.1091}_{-0.0892}$
SAAO I band LDC 2	$q_{2:SAAO_i}$	$0.5, \mathcal{U}(0.0, 1.0)$	$0.6158^{+0.2615}_{-0.3336}$
System Parameters			
Radius ratio	R_b/R_*	$0.116, \mathcal{U}(0.0, 0.3)$	$0.1667^{+0.0011}_{-0.0010}$
Scaled summed radius	$(R_* + R_b)/a_b$	$0.16, \mathcal{U}(0.0, 0.3)$	$0.1579^{+0.0027}_{-0.0024}$
Cosine inclination	$\cos i_b$	$0, \mathcal{U}(0.0, 0.5)$	$0.0808^{+0.0032}_{-0.0030}$
Epoch (BJD)	$T_{0,b}$	$2459360.305123, \mathcal{U}(2459350, 2459370)$	$2458953.9685^{+0.0001}_{-0.0001}$
Orbital Period (d)	P_{orb}	$1.25412, \mathcal{U}(1.245, 1.265)$	$1.2541^{+0.0000}_{-0.0000}$
RV Semi-amplitude (km/s)	K_b	$15, \mathcal{U}(12, 22)$	$18.4107^{+0.2367}_{-0.1659}$
$\sqrt{e_b} \cos \omega_b$	f_c	$0, \mathcal{U}(-1, 1)$	$-0.0289^{+0.0236}_{-0.0173}$
$\sqrt{e_b} \sin \omega_b$	f_s	$0, \mathcal{U}(-1, 1)$	$-0.1981^{+0.0267}_{-0.0156}$
Dilution values			
NGTS Dilution	D_{NGTS}	$0.4364, \mathcal{N}(0.4364, 0.0186)$	$0.4222^{+0.0095}_{-0.0111}$
TESS Dilution	D_{TESS}	$0.4466, \mathcal{N}(0.4466, 0.0156)$	$0.4145^{+0.0089}_{-0.0097}$
SPECULOOS-S I+z' Dilution	$D_{SPEC_{i,zp}}$	-	0.0 (fixed)
SPECULOOS-S z' Dilution	$D_{SPEC_{z,p}}$	-	0.0 (fixed)
SPECULOOS-S g' Dilution	$D_{SPEC_{g,p}}$	-	0.0 (fixed)
SPECULOOS-S i' Dilution	$D_{SPEC_{i,p}}$	$0, \mathcal{U}(0, 1)$	$0.0226^{+0.0191}_{-0.0145}$
SPECULOOS-S r' Dilution	$D_{SPEC_{r,p}}$	-	0.0 (fixed)
TRAPPIST-S I+z' Dilution	$D_{TRAP_{i,zp}}$	$0, \mathcal{U}(0, 1)$	$0.3599^{+0.0268}_{-0.0265}$
TRAPPIST-S z' Dilution	$D_{TRAP_{z,p}}$	$0, \mathcal{U}(0, 1)$	$0.3648^{+0.0268}_{-0.0262}$
SAAO I band Dilution	D_{SAAO_i}	$0, \mathcal{U}(0, 1)$	$0.1791^{+0.0276}_{-0.0269}$
White noise			
-	$\ln \sigma_{NGTS}$	$-5, \mathcal{U}(-10, -1)$	$-5.0915^{+0.0073}_{-0.0073}$
-	$\ln \sigma_{TESS}$	$-5, \mathcal{U}(-10, -1)$	$-5.1962^{+0.0081}_{-0.0078}$
-	$\ln \sigma_{SPEC_{i,zp}}$	$-5, \mathcal{U}(-10, -1)$	$-5.5845^{+0.0230}_{-0.0231}$
-	$\ln \sigma_{SPEC_{z,p}}$	$-5, \mathcal{U}(-10, -1)$	$-5.6716^{+0.0334}_{-0.0328}$
-	$\ln \sigma_{SPEC_{g,p}}$	$-5, \mathcal{U}(-10, -1)$	$-5.6037^{+0.0672}_{-0.0617}$
-	$\ln \sigma_{SPEC_{i,p}}$	$-5, \mathcal{U}(-10, -1)$	$-5.2349^{+0.0304}_{-0.0304}$
-	$\ln \sigma_{SPEC_{r,p}}$	$-5, \mathcal{U}(-10, -1)$	$-5.6961^{+0.0429}_{-0.0435}$
-	$\ln \sigma_{TRAP_{i,zp}}$	$-5, \mathcal{U}(-10, -1)$	$-5.4060^{+0.0345}_{-0.0333}$
-	$\ln \sigma_{TRAP_{z,p}}$	$-5, \mathcal{U}(-10, -1)$	$-5.6070^{+0.0411}_{-0.0411}$
-	$\ln \sigma_{SAAO_i}$	$-5, \mathcal{U}(-10, -1)$	$-4.6564^{+0.0174}_{-0.0172}$
-(km/s)	$\ln \sigma_{jitter} (RV_{HARPS})$	$-2, \mathcal{U}(-4, -1)$	$-2.1615^{+0.5819}_{-0.6698}$
Baseline parameters for GP			
$\ln \sigma_{NGTS}$	offset(NGTS)	$-4.6161, \mathcal{N}(-4.6161, 0.0587)$	$4.5927^{+0.0386}_{-0.0359}$
$\ln \rho_{NGTS}$	offset(NGTS)	$-1.4840, \mathcal{N}(-1.4840, 0.0764)$	$1.6515^{+0.0497}_{-0.0577}$
$\ln \sigma_{TESS}$	offset(TESS)	$-4.4589, \mathcal{N}(-4.4589, 0.1135)$	$4.4356^{+0.0635}_{-0.0582}$
$\ln \rho_{TESS}$	offset(TESS)	$-0.9483, \mathcal{N}(-0.9483, 0.1049)$	$0.9319^{+0.0697}_{-0.0678}$

Table 6. The final DNS derived parameters for NGTS-28Ab, produced by ALLESFITTER. These values are used in future analysis.

Parameter	Value
<i>Derived parameters</i>	
Host radius over semi-major axis b; R_\star/a_b	$0.1353^{+0.0023}_{-0.0020}$
Semi-major axis b over host radius; a_b/R_\star	$7.3872^{+0.1127}_{-0.1210}$
Companion radius b over semi-major axis b; R_b/a_b	$0.0226^{+0.0005}_{-0.0004}$
Companion radius b; R_b (R_{jup})	$0.9534^{+0.0488}_{-0.0484}$
Semi-major axis b; a_b (R_\odot)	$4.3387^{+0.2313}_{-0.2282}$
Semi-major axis b; a_b (AU)	$0.0202^{+0.0011}_{-0.0011}$
Inclination b; i_b (deg)	$85.3628^{+0.1735}_{-0.1863}$
Eccentricity b; e_b	$0.0404^{+0.0067}_{-0.0101}$
Argument of periastron b; w_b (deg)	$261.7232^{+6.7190}_{-4.9514}$
Mass ratio b; q_b	$0.1181^{+0.0077}_{-0.0069}$
Companion mass b; M_b (M_{jup})	$69.0125^{+5.3172}_{-4.8181}$
Companion mass b; M_b (M_\odot)	$0.0659^{+0.0051}_{-0.0046}$
Impact parameter b; $b_{\text{tra},b}$	$0.6200^{+0.0147}_{-0.01367}$
Total transit duration b; $T_{\text{tot},b}$ (h)	$1.3404^{+0.0105}_{-0.0093}$
Full-transit duration b; $T_{\text{full},b}$ (h)	$0.7537^{+0.0117}_{-0.0135}$
Host density from orbit b; $\rho_{\star,b}$ (cgs)	$4.8485^{+0.2253}_{-0.2344}$
Companion density b; ρ_b (cgs)	$98.7270^{+23.9807}_{-18.6470}$
Companion surface gravity b; g_b (cgs)	$210796.5463^{+7782.8359}_{-8754.0340}$
Equilibrium temperature b; $T_{\text{eq},b}$ (K)	$863.2442^{+13.1585}_{-12.5882}$
Transit depth (undil.) b; $\delta_{\text{tr},\text{undil},b;\text{NGTS}_2}$ (ppt)	$30.2106^{+0.7684}_{-0.7502}$
Transit depth (dil.) b; $\delta_{\text{tr},\text{dil},b;\text{NGTS}_2}$ (ppt)	$17.4391^{+0.3714}_{-0.2668}$
Transit depth (undil.) b; $\delta_{\text{tr},\text{undil},b;\text{TESS}_2\text{MIN}}$ (ppt)	$29.8102^{+0.6466}_{-0.6463}$
Transit depth (dil.) b; $\delta_{\text{tr},\text{dil},b;\text{TESS}_2\text{MIN}}$ (ppt)	$17.4538^{+0.2612}_{-0.2484}$
Transit depth (undil.) b; $\delta_{\text{tr},\text{undil},b;\text{SPEC1506},z\text{p}}$ (ppt)	$29.4026^{+0.3149}_{-0.3047}$
Transit depth (dil.) b; $\delta_{\text{tr},\text{dil},b;\text{SPEC1506},z\text{p}}$ (ppt)	$29.4026^{+0.3149}_{-0.3047}$
Transit depth (undil.) b; $\delta_{\text{tr},\text{undil},b;\text{SPEC1506},z\text{p}}$ (ppt)	$29.2768^{+0.3060}_{-0.3085}$
Transit depth (dil.) b; $\delta_{\text{tr},\text{dil},b;\text{SPEC1506},z\text{p}}$ (ppt)	$29.2768^{+0.3060}_{-0.3085}$
Transit depth (undil.) b; $\delta_{\text{tr},\text{undil},b;\text{SPEC1804},g\text{ps},\text{hort}}$ (ppt)	$31.5803^{+0.3587}_{-0.3317}$
Transit depth (dil.) b; $\delta_{\text{tr},\text{dil},b;\text{SPEC1804},g\text{ps},\text{hort}}$ (ppt)	$31.5803^{+0.3587}_{-0.3317}$
Transit depth (undil.) b; $\delta_{\text{tr},\text{undil},b;\text{SPEC1804},p}$ (ppt)	$29.8533^{+0.7533}_{-0.6928}$
Transit depth (dil.) b; $\delta_{\text{tr},\text{dil},b;\text{SPEC1804},p}$ (ppt)	$29.1418^{+0.4886}_{-0.5315}$
Transit depth (undil.) b; $\delta_{\text{tr},\text{undil},b;\text{SPEC1804},r\text{ps},\text{hort}}$ (ppt)	$31.2219^{+0.3354}_{-0.3301}$
Transit depth (dil.) b; $\delta_{\text{tr},\text{dil},b;\text{SPEC1804},r\text{ps},\text{hort}}$ (ppt)	$31.2219^{+0.3354}_{-0.3301}$
Transit depth (undil.) b; $\delta_{\text{tr},\text{undil},b;\text{TRAP1804},z\text{p}}$ (ppt)	$29.3713^{+1.7601}_{-1.6165}$
Transit depth (dil.) b; $\delta_{\text{tr},\text{dil},b;\text{TRAP1804},z\text{p}}$ (ppt)	$18.7979^{+0.7569}_{-0.7499}$
Transit depth (undil.) b; $\delta_{\text{tr},\text{undil},b;\text{TRAP2903},z\text{p}}$ (ppt)	$29.3008^{+1.7784}_{-1.6831}$
Transit depth (dil.) b; $\delta_{\text{tr},\text{dil},b;\text{TRAP2903},z\text{p}}$ (ppt)	$18.5946^{+0.8035}_{-0.7835}$
Transit depth (undil.) b; $\delta_{\text{tr},\text{undil},b;\text{SAAO1s}}$ (ppt)	$29.4383^{+1.4229}_{-1.3570}$
Transit depth (dil.) b; $\delta_{\text{tr},\text{dil},b;\text{SAAO1s}}$ (ppt)	$24.2032^{+0.7457}_{-0.8746}$
Limb darkening; $u_1;\text{NGTS}_2$	$0.3897^{+0.0045}_{-0.0045}$
Limb darkening; $u_2;\text{NGTS}_2$	$0.2823^{+0.0033}_{-0.0035}$
Limb darkening; $u_1;\text{TESS}_2\text{MIN}$	$0.3069^{+0.0029}_{-0.0029}$
Limb darkening; $u_2;\text{TESS}_2\text{MIN}$	$0.2748^{+0.0027}_{-0.0028}$
Limb darkening; $u_1;\text{SPEC1506},z\text{p}$	$0.2100^{+0.0022}_{-0.0022}$
Limb darkening; $u_2;\text{SPEC1506},z\text{p}$	$0.2684^{+0.0026}_{-0.0026}$
Limb darkening; $u_1;\text{SPEC1506},z\text{p}$	$0.1822^{+0.0026}_{-0.0020}$
Limb darkening; $u_2;\text{SPEC1506},z\text{p}$	$0.2666^{+0.0024}_{-0.0023}$
Limb darkening; $u_1;\text{SPEC1804},g\text{ps},\text{hort}$	$0.6173^{+0.0053}_{-0.0050}$
Limb darkening; $u_2;\text{SPEC1804},g\text{ps},\text{hort}$	$0.3265^{+0.0034}_{-0.0033}$
Limb darkening; $u_1;\text{SPEC1804},p$	$0.3188^{+0.0038}_{-0.0035}$
Limb darkening; $u_2;\text{SPEC1804},p$	$0.2768^{+0.0035}_{-0.0035}$
Limb darkening; $u_1;\text{SPEC1804},r\text{ps},\text{hort}$	$0.5583^{+0.0054}_{-0.0057}$
Limb darkening; $u_2;\text{SPEC1804},r\text{ps},\text{hort}$	$0.3244^{+0.0044}_{-0.0043}$
Limb darkening; $u_1;\text{TRAP1804},z\text{p}$	$0.2107^{+0.0048}_{-0.0049}$
Limb darkening; $u_2;\text{TRAP1804},z\text{p}$	$0.2682^{+0.0047}_{-0.0046}$
Limb darkening; $u_1;\text{TRAP2903},z\text{p}$	$0.1823^{+0.0042}_{-0.0039}$
Limb darkening; $u_2;\text{TRAP2903},z\text{p}$	$0.2668^{+0.0047}_{-0.0045}$
Limb darkening; $u_1;\text{SAAO1s}$	$0.5458^{+0.2411}_{-0.2874}$
Limb darkening; $u_2;\text{SAAO1s}$	$-0.1005^{+0.3080}_{-0.2210}$

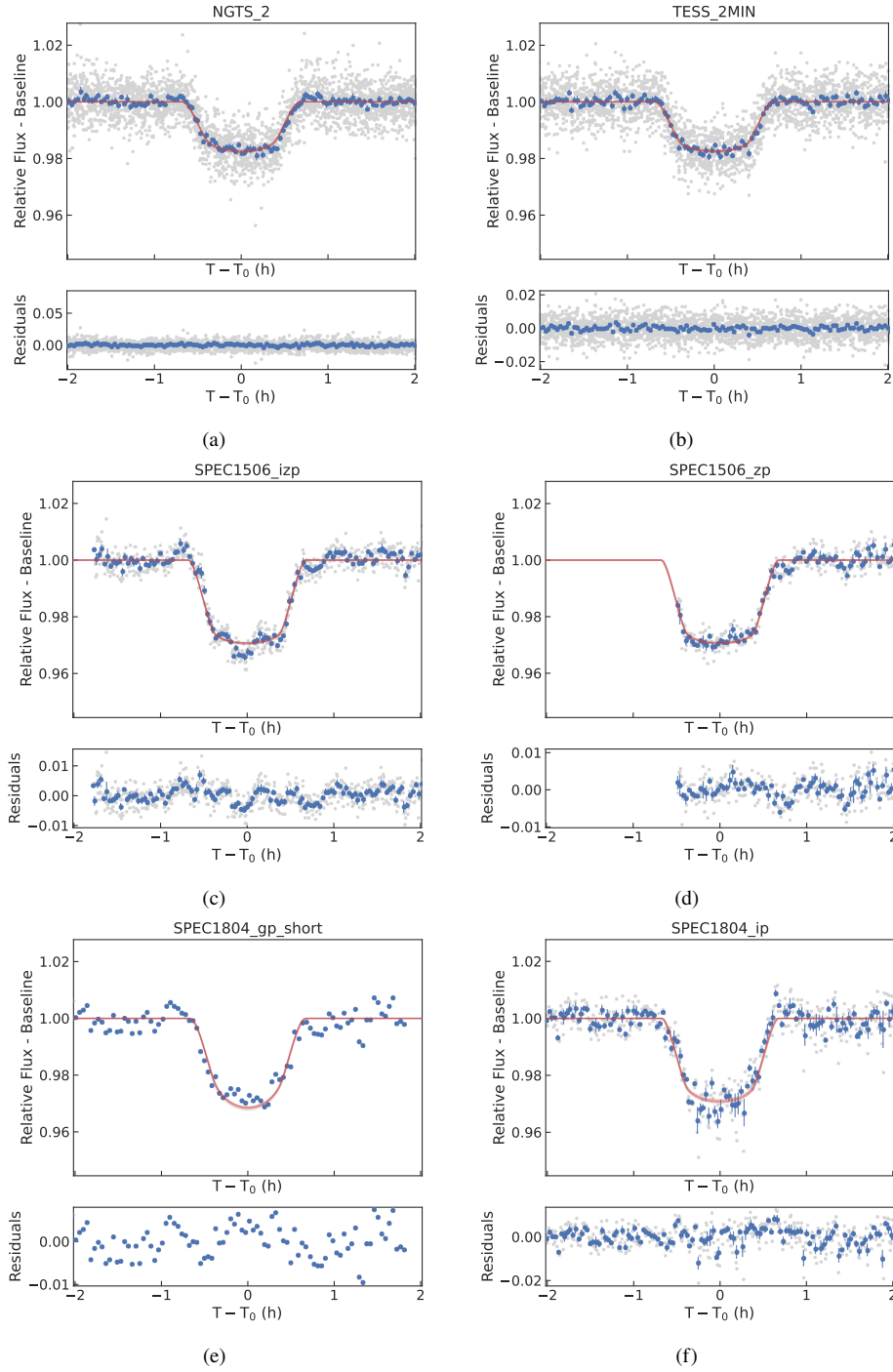


Figure 10. Model fits to (a) NGTS data (binned to 2 minutes), (b) *TESS* 2 minute data, (c) SPECULOOS-S $I + z'$ band data, (d) SPECULOOS-S z' band data, (e) SPECULOOS-S g' band data, (f) SPECULOOS-S g' band data. All model plots are produced with ALLESFITTER. All plots show the inputted data in grey and the 'phased average' flux in blue, with 20 model lines sampled from the posterior.

Where \hat{e} is estimated eccentricity and σ_e is the standard error on the value. Using this relationship from [Lucy & Sweeney \(1971\)](#), our eccentricity is a significant detection.

We expect NGTS-28Ab to be circularised when considering the tidal circularisation timescale. Tidal circularisation is where tidal interactions between a star and its companion cause the orbit to become less eccentric, first discussed in [Zahn & Bouchet \(1989\)](#). From there, objects then undergo rotational and orbital synchronisa-

tion. To calculate an estimate for the circularisation timescale we use Equations (5), (6) and (7) from [Jackson et al. \(2008\)](#).

$$\frac{1}{\tau_{circ,\star}} = \frac{171}{16} \sqrt{\frac{G}{M_\star}} \frac{R_\star^5 M_b}{Q_\star} a^{-\frac{13}{2}}, \quad (5)$$

$$\frac{1}{\tau_{circ,b}} = \frac{63}{4} \sqrt{\frac{GM_\star^3}{Q_b M_b}} \frac{R_b^5}{a^{\frac{13}{2}}}, \quad (6)$$

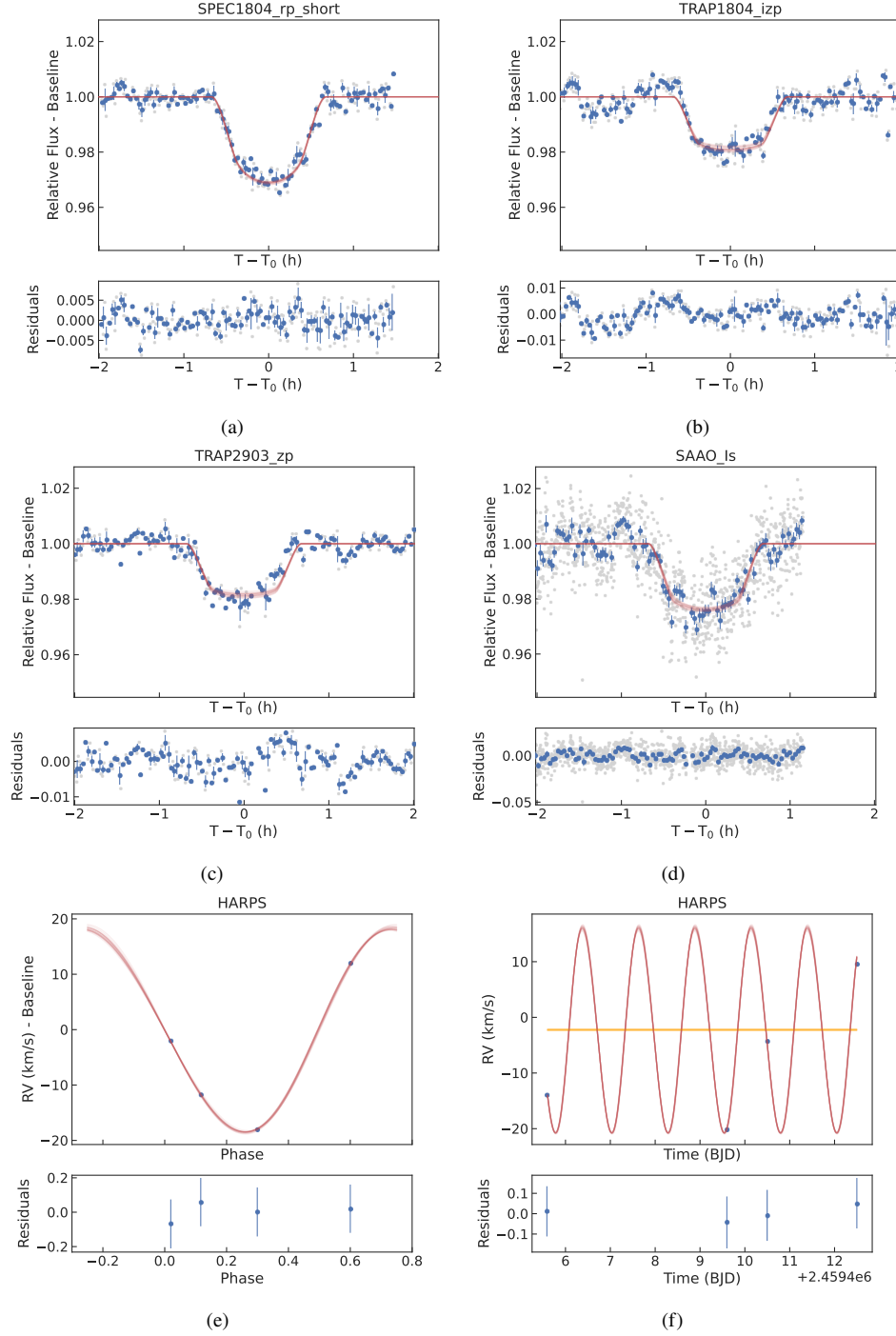


Figure 11. Model fits to (a) SPECULOOS-S i' band data, (b) SPECULOOS-S r' band data, (c) TRAPPIST-S $I + z'$ band data, (d) TRAPPIST-S z' band data, (e) SAO I band data and (f) phasefolded HARPS data (g) timeseries HARPS data. All model plots are produced with ALLESFITTER. All plots show the inputted data in grey and the 'phased average' flux in blue, with 20 model lines sampled from the posterior.

$$\frac{1}{\tau_e} = \frac{1}{\tau_{circ,\star}} + \frac{1}{\tau_{circ,b}}, \quad (7)$$

Where $\tau_{circ,\star}$, $\tau_{circ,b}$ and τ_e are the circularisation timescales for the star, companion and system respectively. G is the gravitational constant, M_\star and M_b are the masses of the star and companion respectively, a is the orbital radius and Q_\star and Q_b are the tidal quality factors. This will estimate a circularisation timescale with

assumptions such as the orbit is not tidally locked, having a period less than 10 d and the eccentricity being low (Jackson et al. 2008).

Using our results and a value of 10^5 for Q_\star (as suggested for M dwarfs in Heller et al. 2010, 2011; Mardling & Lin 2004), we estimated the circularisation timescale for NGTS-28Ab for a range of Q_b values ($10^{4.5}$ to 10^6) following the methods in Carmichael et al. (2020) and Acton et al. (2021). We use a range of values as the tidal quality factor is not well constrained for brown dwarfs. The results can be seen in Table 7. From this test, NGTS-28Ab should have a

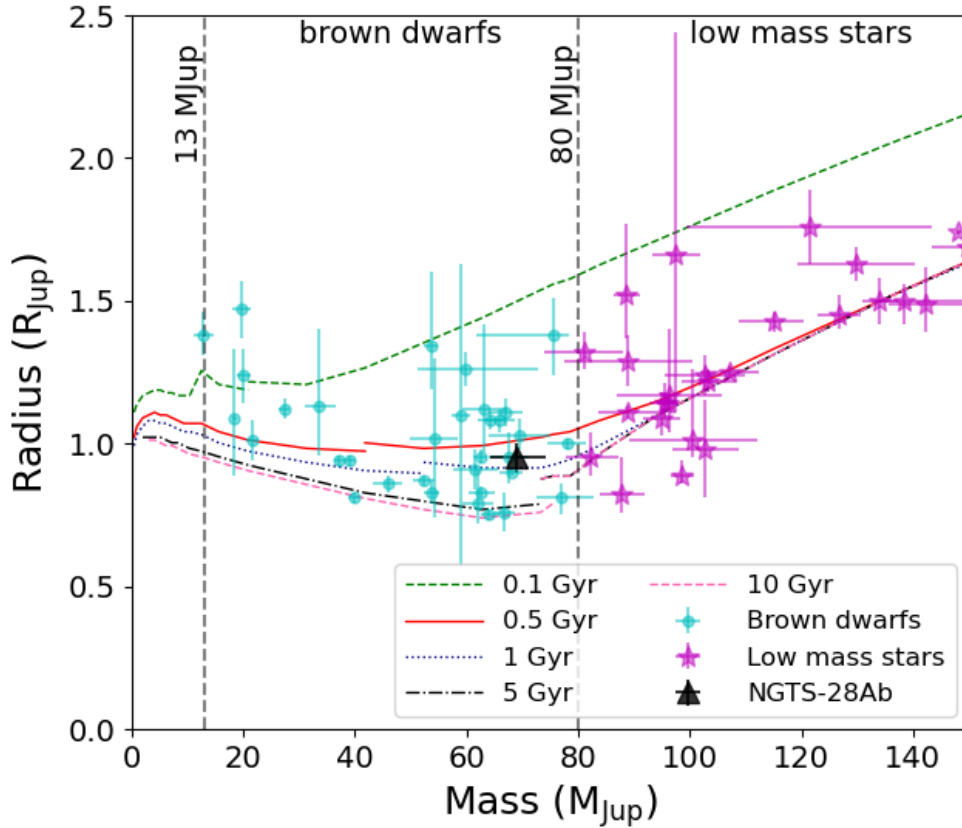


Figure 12. Mass-radius plot for the known transiting brown dwarfs (blue circles) and low mass stars (magenta stars), with NGTS-28Ab (black triangle), adapted from Figure 10 in [Grieves et al. \(2021\)](#). The vertical dashed lines show the upper and lower boundaries of the brown dwarf regime. The lines plotted along the graph show the expected radii of objects at all masses for 0.1 Gyr (green dashed), 0.5 Gyr (red solid), 1 Gyr (blue dotted), 5 Gyr (black dashed-dotted) and 10 Gyr (pink dashed) objects. These isochrones are from [Baraffe et al. 2003, 2015](#). The [Baraffe et al. \(2003\)](#) isochrones are based on the BT-COND models and [Baraffe et al. \(2015\)](#) improve on that with the inclusion of BT-SETTL models ([Allard et al. 2012](#)). The lowest masses of the isochrones are taken from [Baraffe et al. \(2003\)](#). The disconnect in the isochrone lines is due to using the both models. Objects on this plot are listed within Table A1. RIK-72b ([David et al. 2019](#)) and the binary system discovered by [Stassun et al. \(2006\)](#) are not included due to their youth and large radii.

Table 7. Estimated values for tidal circularisation timescale for NGTS-28Ab. These values show a range of possible timescales for Q_b values from $10^{4.5}$ to 10^6 .

Q_b	τ_e (MYr)
$10^{4.5}$	0.96
$10^{4.75}$	0.97
10^5	0.98
$10^{5.25}$	0.99
$10^{5.5}$	0.99
$10^{5.75}$	0.99
10^6	1.00

circularised orbit due to the low timescales, regardless of Q_b value. This is in disagreement to our significant eccentricity detection. With more radial velocity points we may be able to confirm whether the eccentricity is real.

How the object sits within the brown dwarf/low mass star population is important. Figure 13, shows the mass-eccentricity relation for all objects from Table A1. In Figure 13, the objects which are more massive than $42.5 M_J$ (shown by the dotted line), show a flat eccentricity distribution with increasing mass. This is in agreement

with [Ma & Ge \(2014\)](#) and [Grieves et al. \(2017\)](#). NGTS-28Ab lies comfortably within this flat distribution.

From the period-eccentricity plot in Figure 13, it is clear that objects with the highest eccentricities also tend to have long periods. NGTS-28Ab is one of the shortest period transiting brown dwarfs within the desert.

5 CONCLUSION

NGTS-28Ab is a $69.0^{+5.3}_{-4.8} M_J$, $0.95 \pm 0.05 R_J$ brown dwarf, transiting within the sparsely populated brown dwarf desert ([Grether & Lineweaver 2006](#)). Therefore, NGTS-28Ab provides a new opportunity to gain a deeper understanding of this region. The brown dwarf desert is believed to be caused by the minimal overlap of the tail of distributions between planetary and stellar formation mechanisms ([Grieves et al. 2021](#); [Ma & Ge 2014](#)). Therefore, it is important to model parameters that can indicate the formation of each object.

We used spectral fitting and SED fitting methods to analyse the host star NGTS-28A as well as the probable common proper motion companion NGTS-28B ([Mugrauer et al. 2023](#)). We were then able

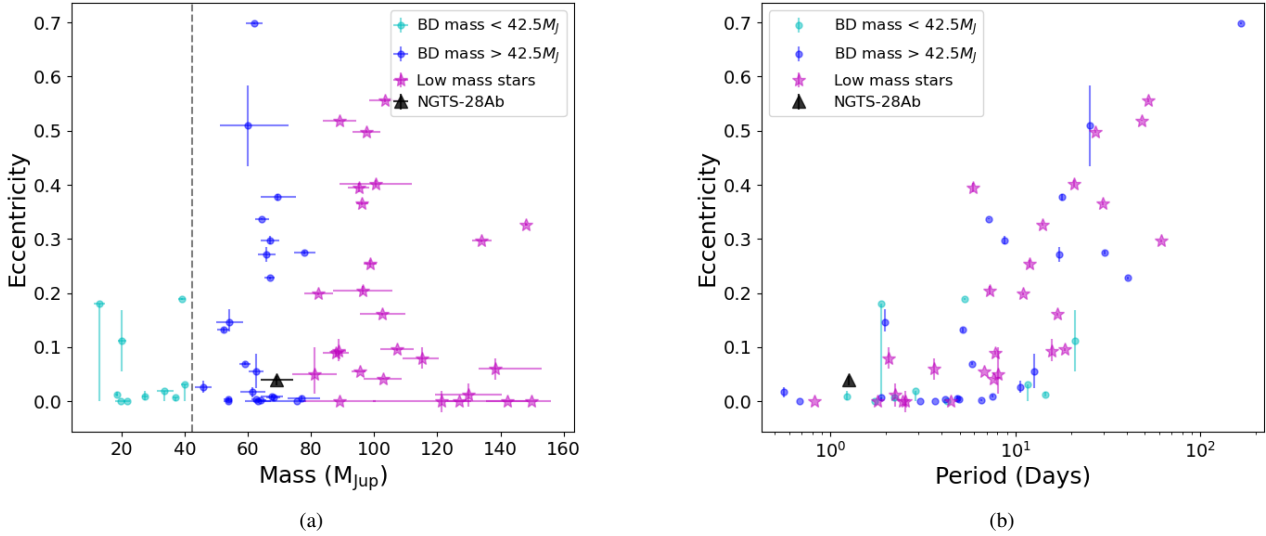


Figure 13. (a): Mass-Eccentricity plot, with a vertical dashed line marking $42.5 M_{\text{J}}$. (b): Period-Eccentricity plot. Both figures show the objects from Table A1 with NGTS-28Ab plotted as an black triangle. Low mass stars are plotted as magenta stars. BDs with masses above $42.5 M_{\text{J}}$ are dark blue circles and BDs with below $42.5 M_{\text{J}}$ are light blue circles. RIK-72b (David et al. 2019) and the binary system discovered by Stassun et al. (2006) are not included due to their youth.

to use the global modelling method ALLESFITTER (Günther & Daylan 2019, 2021) to model the parameters of NGTS-28Ab. Through this we found NGTS-28Ab is likely to have an age > 0.5 Gyrs and has a high mass ratio of $0.1181^{+0.0069}_{-0.0077}$, meaning it likely formed via stellar formation mechanisms, with a low eccentricity value of $0.0404^{+0.0067}_{-0.0101}$.

We found that NGTS-28Ab is orbiting one of the hottest M dwarfs within the transiting BD desert. It is also found to be one of the shortest period transiting brown dwarfs within the desert.

ACKNOWLEDGEMENTS

This work is based on data collected under the NGTS project at the ESO La Silla Paranal Observatory. The NGTS facility is operated by the consortium institutes with support from the UK Science and Technology Facilities Council (STFC) under projects ST/M001962/1, ST/S002642/1 and ST/W003163/1. This study is based on observations collected at the European Southern Observatory under ESO programme 105.20G9. This paper includes public data collected by the TESS mission. Funding for the TESS mission is provided by the NASA Explorer Program. This paper uses observations made at the South African Astronomical Observatory (SAAO). This work has made use of data from the European Space Agency (ESA) mission *Gaia* (<https://www.cosmos.esa.int/gaia>), processed by the *Gaia* Data Processing and Analysis Consortium (DPAC, <https://www.cosmos.esa.int/web/gaia/dpac/consortium>). Funding for the DPAC has been provided by national institutions, in particular, the institutions participating in the *Gaia* Multilateral Agreement.

This publication makes use of data products from the Two Micron All Sky Survey, which is a joint project of the University of Massachusetts and the Infrared Processing and Analysis Center/California Institute of Technology, funded by the National Aeronautics and Space Administration and the National Science Foundation. The Pan-STARRS1 Surveys (PS1) and the PS1 public science

archive have been made possible through contributions by the Institute for Astronomy, the University of Hawaii, the Pan-STARRS Project Office, the Max-Planck Society and its participating institutes, the Max Planck Institute for Astronomy, Heidelberg and the Max Planck Institute for Extraterrestrial Physics, Garching, The Johns Hopkins University, Durham University, the University of Edinburgh, the Queen’s University Belfast, the Harvard-Smithsonian Center for Astrophysics, the Las Cumbres Observatory Global Telescope Network Incorporated, the National Central University of Taiwan, the Space Telescope Science Institute, the National Aeronautics and Space Administration under Grant No. NNX08AR22G issued through the Planetary Science Division of the NASA Science Mission Directorate, the National Science Foundation Grant No. AST-1238877, the University of Maryland, Eotvos Lorand University (ELTE), the Los Alamos National Laboratory, and the Gordon and Betty Moore Foundation.

Some of the Observations in the paper made use of the High-Resolution Imaging instrument Zorro. Zorro was funded by the NASA Exoplanet Exploration Program and built at the NASA Ames Research Center by Steve B. Howell, Nic Scott, Elliott P. Horch, and Emmett Quigley. Zorro was mounted on the Gemini South telescope of the international Gemini Observatory, a program of NSF’s NOIRLab, which is managed by the Association of Universities for Research in Astronomy (AURA) under a cooperative agreement with the National Science Foundation. on behalf of the Gemini partnership: the National Science Foundation (United States), National Research Council (Canada), Agencia Nacional de Investigación y Desarrollo (Chile), Ministerio de Ciencia, Tecnología e Innovación (Argentina), Ministério da Ciência, Tecnologia, Inovações e Comunicações (Brazil), and Korea Astronomy and Space Science Institute (Republic of Korea).

BH is supported by an STFC studentship (ST/S505511/1 and ST/S506242/1). SLC acknowledges support from an STFC Ernest Rutherford Fellowship (ST/R003726/1). The contribution of FB, ML, OT and SU has been carried out within the framework of the NCCR PlanetS supported by the Swiss National Science Founda-

tion under grants 51NF40_182901 and 51NF40_205606. ML acknowledges support of the Swiss National Science Foundation under grant number PCEFP2_194576. The contribution of EMB has been supported by STFC through the consolidated grant ST/W001136/1. CAC acknowledges that this research was carried out at the Jet Propulsion Laboratory, California Institute of Technology, under a contract with NASA (80NM0018D0004). JSJ greatly acknowledges support by FONDECYT grant 1201371 and from the ANID BASAL projects ACE210002 and FB210003. The postdoctoral fellowship of KB is funded by F.R.S.-FNRS grant T.0109.20 and by the Francqui Foundation. This publication benefits from the support of the French Community of Belgium in the context of the FRIA Doctoral Grant awarded to MT. MG is F.R.S.-FNRS Research Director and EJ is F.R.S.-FNRS Senior Research Associate. F.J.P acknowledges financial support from the grant CEX2021-001131-S funded by MCIN/AEI/ 10.13039/501100011033 and through projects PID2019-109522GB-C52 and PID2022-137241NB-C43. This research is in part funded by the European Union's Horizon 2020 research and innovation programme (grant's agreement n° 803193/BEBOP), from the MERAC foundation, and from the Science and Technology Facilities Council (STFC; grant n° ST/S00193X/1, and ST/W000385/1). Based on data collected by the SPECULOOS-South Observatory at the ESO Paranal Observatory in Chile. The ULiege's contribution to SPECULOOS has received funding from the European Research Council under the European Union's Seventh Framework Programme (FP/2007-2013) (grant Agreement n° 336480/SPECULOOS), from the Balzan Prize and Francqui Foundations, from the Belgian Scientific Research Foundation (F.R.S.-FNRS; grant n° T.0109.20), from the University of Liege, and from the ARC grant for Concerted Research Actions financed by the Wallonia-Brussels Federation. This work is supported by a grant from the Simons Foundation (PI Queloz, grant number 327127). Based on data collected by the TRAPPIST-South telescope at the ESO La Silla Observatory. TRAPPIST is funded by the Belgian Fund for Scientific Research (Fond National de la Recherche Scientifique, FNRS) under the grant PDR T.0120.21, with the participation of the Swiss National Science Foundation (SNF).

DATA AVAILABILITY

The *TESS* data is available via the MAST (Mikulski Archive for Space Telescopes) portal at <https://mast.stsci.edu/portal/Mashup/Clients/Mast/Portal.html>. Data can also be downloaded from TFOP for NGTS-28A (TOI-6110) at <https://exofop.ipac.caltech.edu/tess/target.php?id=7439480>. Public NGTS and HARPS data is available in the ESO archive at http://archive.eso.org/eso/eso_archive_main.html. SAAO data is available on its public archive at <https://ssda.sao.ac.za/>. The other data within this article will be shared on reasonable request to the corresponding author.

SPECMATCH-EMP, ARIADNE and ALLESFITTER are open-source and public software.

REFERENCES

- Acton J. S., et al., 2021, *MNRAS*, 505, 2741–2752
- Allard F., Homeier D., Freytag B., 2012, *Philosophical Transactions of the Royal Society of London Series A*, 370, 2765
- Alves D. R., et al., 2022, *MNRAS*,
- Artigau É., et al., 2021, *AJ*, 162, 144
- Astropy Collaboration et al., 2013, *A&A*, 558, A33
- Astropy Collaboration et al., 2018, *AJ*, 156, 123
- Astropy Collaboration et al., 2022, *apj*, 935, 167
- Baraffe I., Chabrier G., Allard F., Hauschildt P. H., 2002, *A&A*, 382, 563
- Baraffe I., Chabrier G., Barman T. S., Allard F., Hauschildt P. H., 2003, *A&A*, 402, 701
- Baraffe I., Homeier D., Allard F., Chabrier G., 2015, *A&A*, 577, A42
- Baranne A., et al., 1996, *A&AS*, 119, 373
- Barkaoui K., et al., 2023, *A&A*, 677, A38
- Bate M. R., Bonnell I. A., Bromm V., 2002, *MNRAS*, 332, L65
- Bayliss D., et al., 2017, *AJ*, 153, 15
- Beatty T. G., et al., 2007, *ApJ*, 663, 573
- Beatty T. G., et al., 2014, *ApJ*, 783, 112
- Benni P., et al., 2021, *MNRAS*, 505, 4956
- Bonomo A. S., et al., 2015, *A&A*, 575, A85
- Bouchy F., et al., 2011, *A&A*, 525, A68
- Bowler B. P., Blunt S. C., Nielsen E. L., 2020, *AJ*, 159, 63
- Broeg C., Fernández M., Neuhäuser R., 2005, *Astronomische Nachrichten*, 326, 134
- Burgasser A. J., 2008, *Physics Today*, 61, 70
- Burrows A., Liebert J., 1993, *Reviews of Modern Physics*, 65, 301
- Carmichael T. W., Latham D. W., Vanderburg A. M., 2019, *AJ*, 158, 38
- Carmichael T. W., et al., 2020, *AJ*, 160, 53
- Carmichael T. W., et al., 2021, *AJ*, 161, 97
- Carmichael T. W., et al., 2022, *MNRAS*, 514, 4944
- Casewell S. L., et al., 2020a, *MNRAS*, 497, 3571
- Casewell S. L., Debes J., Braker I. P., Cushing M. C., Mace G., Marley M. S., Kirkpatrick J. D., 2020b, *MNRAS*, 499, 5318
- Castelli F., Kurucz R., 2004, *Proceedings of the International Astronomical Union*
- Chambers K. C., et al., 2016, arXiv e-prints, [p. arXiv:1612.05560](https://arxiv.org/abs/1612.05560)
- Chaturvedi P., Chakraborty A., Anandarao B. G., Roy A., Mahadevan S., 2016, *MNRAS*, 462, 554
- Chaturvedi P., Sharma R., Chakraborty A., Anandarao B. G., Prasad N. J. S. S. V., 2018, *AJ*, 156, 27
- Ciardi D. R., Beichman C. A., Horch E. P., Howell S. B., 2015, *ApJ*, 805, 16
- Coppejans R., et al., 2013, *PASP*, 125, 976
- Csizmadia S., 2016, in , *The CoRoT Legacy Book*. EDP Sciences, p. 143, doi:10.1051/978-2-7598-1876-1.c036, <https://doi.org/10.1051/978-2-7598-1876-1.c036>
- Csizmadia S., et al., 2015, *A&A*, 584, A13
- Dall T. H., Santos N. C., Arentoft T., Bedding T. R., Kjeldsen H., 2006, *A&A*, 454, 341
- David T. J., Hillenbrand L. A., Gillen E., Cody A. M., Howell S. B., Isaacson H. T., Livingston J. H., 2019, *ApJ*, 872, 161
- Deleuil M., et al., 2008, *A&A*, 491, 889
- Delrez L., et al., 2018, in *Ground-based and Airborne Telescopes VII*. pp 446–466
- Díaz R. F., et al., 2013, *A&A*, 551, L9
- Díaz R. F., et al., 2014, *A&A*, 572, A109
- Dransfield G., et al., 2024, *MNRAS*, 527, 35
- Eaton N., Draper P. W., Allan A., Naylor T., Mukai K., Currie M. J., McCaughrean M., 2014, *PHOTOM: Photometry of digitized images*, Astrophysics Source Code Library, record ascl:1405.013 (ascl:1405.013)
- Flewelling H. A., et al., 2020, *ApJS*, 251, 7
- Foreman-Mackey D., Hogg D. W., Lang D., Goodman J., 2013, *PASP*, 125, 306
- Furlan E., Howell S. B., 2017, *AJ*, 154, 66
- Gagné J., et al., 2018, *ApJ*, 856, 23
- Gaia Collaboration et al., 2016, *A&A*, 595, A1
- Gaia Collaboration et al., 2022, arXiv e-prints, [p. arXiv:2208.00211](https://arxiv.org/abs/2208.00211)
- García L. J., Timmermans M., Pozuelos F. J., Ducrot E., Gillon M., Delrez L., Wells R. D., Jehin E., 2022, *MNRAS*, 509, 4817
- Gill S., et al., 2020, *MNRAS*, 495, 2713
- Gill S., et al., 2022, *MNRAS*, 513, 1785
- Gillen E., Hillenbrand L. A., David T. J., Aigrain S., Rebull L., Stauffer J., Cody A. M., Queloz D., 2017, *ApJ*, 849, 11
- Gillon M., Jehin E., Magain P., Chantry V., Hutsemékers D., Manfroid J., Queloz D., Udry S., 2011, in *European Physi-*

- cal Journal Web of Conferences. p. 06002 ([arXiv:1101.5807](https://arxiv.org/abs/1101.5807)), [doi:10.1051/epjconf/20101106002](https://doi.org/10.1051/epjconf/20101106002)
- Grether D., Lineweaver C. H., 2006, *ApJ*, **640**, 1051
- Grievies N., et al., 2017, *MNRAS*, **467**, 4264
- Grievies N., et al., 2021, *A&A*, **652**, A127
- Günther M. N., Daylan T., 2019, *Allesfitter: Flexible Star and Exoplanet Inference From Photometry and Radial Velocity*, Astrophysics Source Code Library (ascl:1903.003)
- Günther M. N., Daylan T., 2021, *ApJS*, **254**, 13
- Günther M. N., et al., 2018, *MNRAS*, **478**, 4720
- Hauschildt P. H., Allard F., Baron E., 1999, *ApJ*, **512**, 377
- Heller R., Jackson B., Barnes R., Greenberg R., Homeier D., 2010, *A&A*, **514**, A22
- Heller R., Leconte J., Barnes R., 2011, *A&A*, **528**, A27
- Hodžić V., et al., 2018, *MNRAS*, **481**, 5091
- Howell S. B., Furlan E., 2022, *Frontiers in Astronomy and Space Sciences*, **9**
- Howell S. B., Everett M. E., Sherry W., Horch E., Ciardi D. R., 2011, *AJ*, **142**, 19
- Husser T. O., Wende-von Berg S., Dreizler S., Homeier D., Reiners A., Barman T., Hauschildt P. H., 2013, *A&A*, **553**, A6
- Irwin J., et al., 2010, *ApJ*, **718**, 1353
- Irwin J. M., et al., 2018, *AJ*, **156**, 140
- Jackman J. A. G., et al., 2019, *MNRAS*, **489**, 5146
- Jackson B., Greenberg R., Barnes R., 2008, *ApJ*, **678**, 1396
- Jeffreys H., 1998, *The Theory of Probability*. Oxford Classic Texts in the Physical Sciences, OUP Oxford, <https://books.google.co.uk/books?id=vh9Act9rtzQC>
- Jehin E., et al., 2011, *The Messenger*, **145**, 2
- Jehin E., et al., 2018, *The Messenger*, **174**, 2
- Jenkins J. S., et al., 2015, *MNRAS*, **453**, 1439
- Jenkins J. M., et al., 2016, in Chiozzi G., Guzman J. C., eds, *Society of Photo-Optical Instrumentation Engineers (SPIE) Conference Series Vol. 9913, Software and Cyberinfrastructure for Astronomy IV*. p. 99133E, [doi:10.1117/12.2233418](https://doi.org/10.1117/12.2233418)
- Johnson J. A., et al., 2011, *ApJ*, **730**, 79
- Kass R. E., Raftery A. E., 1995, *Journal of the American Statistical Association*, **90**, 773
- Kipping D. M., 2013, *MNRAS*, **435**, 2152
- Kurucz R., 1993, *ATLAS9 Stellar Atmosphere Programs and 2 km/s grid*. Kurucz CD-ROM No. 13. Cambridge, 13
- Latham D. W., Mazeh T., Stefanik R. P., Mayor M., Burki G., 1989, *Nature*, **339**, 38
- Lomb N. R., 1976, *Ap&SS*, **39**, 447
- Lucy L. B., Sweeney M. A., 1971, *AJ*, **76**, 544
- Ma B., Ge J., 2014, *MNRAS*, **439**, 2781
- Mardling R. A., Lin D. N. C., 2004, *ApJ*, **614**, 955
- Marley M. S., et al., 2021, *ApJ*, **920**, 85
- Maxted P. F. L., 2016, *A&A*, **591**, A111
- Mayor M., et al., 2003, *The Messenger*, **114**, 20
- Mireles I., et al., 2020, *AJ*, **160**, 133
- Moutou C., et al., 2013, *A&A*, **558**, L6
- Mugrauer M., Rück J., Michel K. U., 2023, *arXiv e-prints*, p. [arXiv:2306.02452](https://arxiv.org/abs/2306.02452)
- Nakajima T., Oppenheimer B. R., Kulkarni S. R., Golimowski D. A., Matthews K., Durrance S. T., 1995, *Nature*, **378**, 463
- Nefs S. V., et al., 2013, *MNRAS*, **431**, 3240
- Nowak G., et al., 2017, *AJ*, **153**, 131
- Ofir A., Gandolfi D., Buchhave L., Lacy C. H. S., Hatzes A. P., Fridlund M., 2012, *MNRAS*, **423**, L1
- Palle E., et al., 2021, *A&A*, **650**, A55
- Parsons S. G., et al., 2018, *MNRAS*, **481**, 1083
- Parviainen H., Aigrain S., 2015, *MNRAS*, **453**, 3821
- Parviainen H., et al., 2020, *A&A*, **633**, A28
- Pecaat M. J., Mamajek E. E., 2013, *ApJS*, **208**, 9
- Pepe F., Mayor M., Galland F., Naef D., Queloz D., Santos N. C., Udry S., Burnet M., 2002, *A&A*, **388**, 632
- Persson C. M., et al., 2019, *A&A*, **628**, A64
- Pont F., Melo C. H. F., Bouchy F., Udry S., Queloz D., Mayor M., Santos N. C., 2005a, *A&A*, **433**, L21
- Pont F., Bouchy F., Melo C., Santos N. C., Mayor M., Queloz D., Udry S., 2005b, *A&A*, **438**, 1123
- Pont F., et al., 2006, *A&A*, **447**, 1035
- Psaridi A., et al., 2022, *A&A*, **664**, A94
- Queloz D., et al., 2001, *A&A*, **379**, 279
- Raghavan D., et al., 2010, *Astrophysical Journal, Supplement Series*, **190**, 1
- Rajpurohit A. S., Reylé C., Allard F., Homeier D., Schultheis M., Bessell M. S., Robin A. C., 2013, *A&A*, **556**, A15
- Rebolo R., Zapatero Osorio M. R., Martín E. L., 1995, *Nature*, **377**, 129
- Ricker G. R., et al., 2014, *Journal of Astronomical Telescopes, Instruments, and Systems*, **1**, 1
- STScI Development Team 2013, *pysynphot: Synthetic photometry software package*, Astrophysics Source Code Library, record ascl:1303.023 (ascl:1303.023)
- Santos N. C., et al., 2002, *A&A*, **392**, 215
- Scargle J. D., 1982, *ApJ*, **263**, 835
- Schafferoth V., et al., 2021, *MNRAS*, **501**, 3847
- Science Software Branch at STScI 2012, *PyRAF: Python alternative for IRAF*, Astrophysics Source Code Library, record ascl:1207.011 (ascl:1207.011)
- Scott N. J., et al., 2021, *Frontiers in Astronomy and Space Sciences*, **8**
- Sebastian D., et al., 2021, *A&A*, **645**, A100
- Shporer A., et al., 2017, *ApJ*, **847**, L18
- Sivverid R. J., et al., 2012, *ApJ*, **761**, 123
- Skrutskie M. F., et al., 2006, *AJ*, **131**, 1163
- Speagle J. S., 2020, *MNRAS*, **493**, 3132
- Stassun K. G., Mathieu R. D., Valenti J. A., 2006, *Nature*, **440**, 311
- Tal-Or L., et al., 2013, *A&A*, **553**, A30
- Tamaz O., Mazeh T., Zucker S., 2005, *MNRAS*, **356**, 1466
- Thorngren D. P., Fortney J. J., Lopez E. D., Berger T. A., Huber D., 2021, *ApJ*, **909**, L16
- Tilbrook R. H., et al., 2021, *MNRAS*, **504**, 6018
- Tody D., 1986, in Crawford D. L., ed., *Society of Photo-Optical Instrumentation Engineers (SPIE) Conference Series Vol. 627, Instrumentation in astronomy VI*. p. 733, [doi:10.1117/12.968154](https://doi.org/10.1117/12.968154)
- Tody D., 1993, in Hanisch R. J., Brissenden R. J. V., Barnes J., eds, *Astronomical Society of the Pacific Conference Series Vol. 52, Astronomical Data Analysis Software and Systems II*. p. 173
- TriAUD A. H. M. J., et al., 2013, *A&A*, **549**, A18
- TriAUD A. H. M. J., et al., 2017, *A&A*, **608**, A129
- TriAUD A. H. M. J., et al., 2020, *Nature*, **4**, 650
- Vines J. I., Jenkins J. S., 2022, *MNRAS*,
- Wheatley P. J., et al., 2018, *MNRAS*, **475**, 4476
- Whitworth A., 2018, *arXiv e-prints*, p. [arXiv:1811.06833](https://arxiv.org/abs/1811.06833)
- Yee S. W., Petigura E. A., von Braun K., 2017, *ApJ*, **836**, 77
- Zahn J. P., Bouchet L., 1989, *A&A*, **223**, 112
- Zhou G., et al., 2014, *MNRAS*, **437**, 2831
- Zhou G., et al., 2019, *AJ*, **157**, 31
- Šubjak J., et al., 2020, *AJ*, **159**, 151
- von Boetticher A., et al., 2017, *A&A*, **604**, L6
- von Boetticher A., et al., 2019, *A&A*, **625**, A150

APPENDIX A: EXTRA DATA, FIGURES AND TABLES

A1 Full Data Tables

A2 Corner Plots

A3 Brown Dwarf Desert Population Plots

This paper has been typeset from a $\text{\TeX}/\text{\LaTeX}$ file prepared by the author.

Table A1. Parameters of all objects used within the population analysis. RIK-72b (David et al. 2019) and the binary system discovered by Stassun et al. (2006) are not included due to their youth and large radii. Table has been adapted and updated from Grieves et al. (2021). Sources: (1): Zhou et al. (2019), (2): Artigau et al. (2021), (3): Benni et al. (2021), (4): Bonomo et al. (2015), (5): Deleuil et al. (2008), (6): Siverd et al. (2012), (7): Beatty et al. (2014), (8): Irwin et al. (2010), (9): Csizmadia (2016), (10): Hodžić et al. (2018), (11): Nowak et al. (2017), (12): Carmichael et al. (2019), (13): Díaz et al. (2013), (14): Carmichael et al. (2020), (15): Persson et al. (2019), (16): Šubjak et al. (2020), (17): Carmichael et al. (2021), (18): Gillen et al. (2017), (19): Csizmadia et al. (2015), (20): Parviainen et al. (2020), (21): Palle et al. (2021), (22): Moutou et al. (2013), (23): Triaud et al. (2013), (24): Johnson et al. (2011), (25): Bouchy et al. (2011), (26): Carmichael et al. (2022), (27): Psaridi et al. (2022), (28): Bayliss et al. (2017), (29): Irwin et al. (2018), (30): Acton et al. (2021), (31): Jackman et al. (2019), (32): Grieves et al. (2021), (33): Díaz et al. (2014), (34): von Boettcher et al. (2017), (35): von Boettcher et al. (2019), (36): Pont et al. (2006), (37): Mireles et al. (2020), (38): Gill et al. (2022), (39): Pont et al. (2005a), (40): Shporer et al. (2017), (41): Tal-Or et al. (2013), (42): Chaturvedi et al. (2016), (43): Zhou et al. (2014), (44): Pont et al. (2005b), (45): Beatty et al. (2007), (46): Gill et al. (2020), (47): Ofir et al. (2012), (48): Neffs et al. (2013).

Object	P [d]	M ₂ [M _J]	R ₂ [R _J]	T _{eff} [K]	M ₁ [M _☉]	R ₁ [R _☉]	ecc	[Fe/H]	Source
HATS-70b	1.89	12.9 ^{+1.8} _{-1.8}	1.38 ^{+0.08} _{-0.07}	7930 ⁺⁶³⁰ ₋₈₂₀	1.78 ^{+0.12} _{-0.12}	1.88 ^{+0.06} _{-0.07}	< 0.18	0.04 ^{+0.10} _{-0.10}	(1)
TOI-1278b	14.48	18.5 ^{+0.5} _{-0.5}	1.09 ^{+0.27} _{-0.20}	3799 ⁺⁴² ₋₄₂	0.55 ^{+0.02} _{-0.02}	0.57 ^{+0.01} _{-0.01}	0.013 ^{+0.004} _{-0.004}	-0.01 ^{+0.28} _{-0.28}	(2)
GPX-1b	1.74	19.7 ^{+1.6} _{-1.6}	1.47 ^{+0.10} _{-0.10}	7000 ⁺²⁰⁰ ₋₂₀₀	1.68 ^{+0.10} _{-0.10}	1.56 ^{+0.10} _{-0.10}	0 (fixed)	0.35 ^{+0.10} _{-0.10}	(3)
Kepler-39b	21.09	20.1 ^{+1.3} _{-1.2}	1.24 ^{+0.09} _{-0.10}	6350 ⁺¹⁰⁰ ₋₁₀₀	1.29 ^{+0.06} _{-0.07}	1.40 ^{+0.10} _{-0.10}	0.112 ^{+0.057} _{-0.057}	0.10 ^{+0.14} _{-0.14}	(4)
CoRoT-3b	4.26	21.7 ^{+1.0} _{-1.0}	1.01 ^{+0.07} _{-0.07}	6740 ⁺¹⁴⁰ ₋₁₄₀	1.37 ^{+0.09} _{-0.09}	1.56 ^{+0.09} _{-0.09}	0 (fixed)	-0.02 ^{+0.06} _{-0.06}	(5)
KELT-1b	1.22	27.4 ^{+0.9} _{-0.9}	1.12 ^{+0.04} _{-0.03}	6516 ⁺⁴⁹ ₋₄₉	1.34 ^{+0.06} _{-0.06}	1.47 ^{+0.05} _{-0.04}	0.010 ^{+0.010} _{-0.007}	0.05 ^{+0.08} _{-0.08}	(6)(7)
NLTT41135b	2.89	33.7 ^{+2.8} _{-2.6}	1.13 ^{+0.27} _{-0.17}	3230 ⁺¹³⁰ ₋₁₃₀	0.19 ^{+0.03} _{-0.02}	0.21 ^{+0.02} _{-0.01}	< 0.02	0 (fixed)	(8)(9)
WASP-128b	2.21	37.2 ^{+0.8} _{-0.9}	0.94 ^{+0.02} _{-0.02}	5950 ⁺⁵⁰ ₋₅₀	1.16 ^{+0.04} _{-0.04}	1.15 ^{+0.02} _{-0.02}	< 0.007	0.01 ^{+0.12} _{-0.12}	(10)
CWW89Ab	5.29	39.2 ^{+1.1} _{-1.1}	0.94 ^{+0.02} _{-0.02}	5755 ⁺⁴⁹ ₋₄₉	1.10 ^{+0.05} _{-0.05}	1.03 ^{+0.02} _{-0.02}	0.189 ^{+0.002} _{-0.002}	0.20 ^{+0.09} _{-0.09}	(11)(12)
KOI-205b	11.72	39.9 ^{+1.0} _{-1.0}	0.81 ^{+0.02} _{-0.02}	5237 ⁺⁶⁰ ₋₆₀	0.93 ^{+0.03} _{-0.03}	0.84 ^{+0.02} _{-0.02}	< 0.031	0.14 ^{+0.12} _{-0.12}	(13)
TOI-1406b	10.57	46.0 ^{+2.6} _{-2.7}	0.86 ^{+0.03} _{-0.03}	6290 ⁺¹⁰⁰ ₋₁₀₀	1.18 ^{+0.08} _{-0.09}	1.35 ^{+0.03} _{-0.03}	0.026 ^{+0.013} _{-0.010}	-0.08 ^{+0.09} _{-0.09}	(14)
EPIC212036875b	5.17	52.3 ^{+1.9} _{-1.9}	0.87 ^{+0.02} _{-0.02}	6238 ⁺⁵⁹ ₋₆₀	1.29 ^{+0.07} _{-0.06}	1.50 ^{+0.03} _{-0.03}	0.132 ^{+0.004} _{-0.004}	0.01 ^{+0.10} _{-0.10}	(12)(15)
TOI-503b	3.68	53.7 ^{+1.2} _{-1.2}	1.34 ^{+0.26} _{-0.15}	7650 ⁺¹⁴⁰ ₋₁₆₀	1.80 ^{+0.06} _{-0.06}	1.70 ^{+0.05} _{-0.04}	0 (fixed)	0.30 ^{+0.08} _{-0.09}	(16)
TOI-852b	4.95	53.7 ^{+1.4} _{-1.3}	0.83 ^{+0.04} _{-0.04}	5768 ⁺⁸⁴ ₋₈₁	1.32 ^{+0.05} _{-0.04}	1.71 ^{+0.04} _{-0.04}	0.004 ^{+0.004} _{-0.003}	0.33 ^{+0.09} _{-0.09}	(17)
AD3116b	1.98	54.2 ^{+4.3} _{-4.3}	1.02 ^{+0.28} _{-0.28}	3184 ⁺²⁹ ₋₂₉	0.28 ^{+0.02} _{-0.02}	0.29 ^{+0.08} _{-0.08}	0.146 ^{+0.024} _{-0.016}	0 (fixed)	(18)
CoRoT-33b	5.82	59.0 ^{+1.8} _{-1.7}	1.10 ^{+0.53} _{-0.53}	5225 ⁺⁸⁰ ₋₈₀	0.86 ^{+0.04} _{-0.04}	0.94 ^{+0.14} _{-0.08}	0.070 ^{+0.002} _{-0.002}	0.44 ^{+0.10} _{-0.10}	(19)
TOI-811b	25.17	59.9 ^{+13.0} _{-8.6}	1.26 ^{+0.06} _{-0.06}	6107 ⁺⁷⁷ ₋₇₇	1.32 ^{+0.05} _{-0.07}	1.27 ^{+0.06} _{-0.09}	0.509 ^{+0.075} _{-0.075}	0.40 ^{+0.07} _{-0.09}	(17)
TOI-263b	0.56	61.6 ^{+4.0} _{-4.0}	0.91 ^{+0.07} _{-0.07}	3471 ⁺³³ ₋₃₃	0.44 ^{+0.04} _{-0.04}	0.44 ^{+0.03} _{-0.03}	0.017 ^{+0.009} _{-0.010}	0.00 ^{+0.10} _{-0.10}	(20)(21)
KOI-415b	166.79	62.1 ^{+2.7} _{-2.7}	0.79 ^{+0.12} _{-0.07}	5810 ⁺⁸⁰ ₋₈₀	0.94 ^{+0.06} _{-0.06}	1.25 ^{+0.15} _{-0.10}	0.698 ^{+0.002} _{-0.002}	-0.24 ^{+0.11} _{-0.11}	(22)
WASP-30b	4.16	62.5 ^{+1.2} _{-1.2}	0.95 ^{+0.03} _{-0.02}	6202 ⁺⁴² ₋₅₁	1.25 ^{+0.03} _{-0.04}	1.39 ^{+0.03} _{-0.03}	< 0.004	0.08 ^{+0.07} _{-0.05}	(23)
LHS6343c	12.71	62.7 ^{+2.4} _{-2.4}	0.83 ^{+0.02} _{-0.02}	3130 ⁺²⁰ ₋₂₀	0.37 ^{+0.01} _{-0.01}	0.38 ^{+0.01} _{-0.01}	0.056 ^{+0.032} _{-0.032}	0.04 ^{+0.08} _{-0.08}	(24)
CoRoT-15b	3.06	63.3 ^{+4.1} _{-4.1}	1.12 ^{+0.30} _{-0.15}	6350 ⁺²⁰⁰ ₋₂₀₀	1.32 ^{+0.12} _{-0.12}	1.46 ^{+0.31} _{-0.14}	0 (fixed)	0.10 ^{+0.20} _{-0.20}	(25)
TOI-569b	6.56	64.1 ^{+1.9} _{-1.4}	0.75 ^{+0.02} _{-0.02}	5768 ⁺¹¹⁰ ₋₉₂	1.21 ^{+0.05} _{-0.05}	1.48 ^{+0.03} _{-0.03}	0.002 ^{+0.002} _{-0.001}	0.29 ^{+0.09} _{-0.08}	(14)
TOI-2119b	7.20	64.4 ^{+2.3} _{-2.2}	1.08 ^{+0.03} _{-0.03}	3621 ⁺⁴⁸ ₋₄₆	0.53 ^{+0.02} _{-0.02}	0.50 ^{+0.02} _{-0.02}	0.337 ^{+0.002} _{-0.001}	0.06 ^{+0.08} _{-0.08}	(26)
TOI-1982b	17.17	65.9 ^{+2.8} _{-2.7}	1.08 ^{+0.04} _{-0.04}	6325 ⁺¹¹⁰ ₋₁₁₀	1.41 ^{+0.08} _{-0.08}	1.51 ^{+0.05} _{-0.05}	0.272 ^{+0.014} _{-0.014}	-0.10 ^{+0.09} _{-0.09}	(27)
NGTS-28Ab	1.25	69.0 ^{+5.3} _{-4.8}	0.95 ± 0.05	3626 ⁺⁴⁷ ₋₄₄	0.56 ^{+0.02} _{-0.02}	0.59 ^{+0.03} _{-0.03}	0.040 ^{+0.007} _{-0.007}	-0.14 ^{+0.16} _{-0.16}	This work
EPIC201702477b	40.74	66.9 ^{+1.7} _{-1.7}	0.76 ^{+0.07} _{-0.07}	5517 ⁺⁷⁰ ₋₇₀	0.87 ^{+0.03} _{-0.03}	0.90 ^{+0.06} _{-0.06}	0.228 ^{+0.003} _{-0.003}	-0.16 ^{+0.05} _{-0.05}	(28)
TOI-629b	8.72	67.0 ^{+3.0} _{-3.0}	1.11 ^{+0.05} _{-0.05}	9100 ⁺²⁰⁰ ₋₂₀₀	2.16 ^{+0.13} _{-0.13}	2.37 ^{+0.11} _{-0.11}	0.298 ^{+0.008} _{-0.008}	0.10 ^{+0.15} _{-0.15}	(27)
TOI-2543b	7.54	67.6 ^{+3.5} _{-3.5}	0.95 ^{+0.09} _{-0.09}	6060 ⁺⁸² ₋₈₂	1.29 ^{+0.08} _{-0.08}	1.86 ^{+0.15} _{-0.15}	0.009 ^{+0.003} _{-0.002}	-0.28 ^{+0.10} _{-0.10}	(27)
LP261-75b	1.88	68.1 ^{+2.1} _{-2.1}	0.90 ^{+0.01} _{-0.01}	3100 ⁺⁵⁰ ₋₅₀	0.30 ^{+0.02} _{-0.02}	0.31 ^{+0.00} _{-0.00}	< 0.007	-	(29)
NGTS-19b	17.84	69.5 ^{+5.7} _{-5.4}	1.03 ^{+0.06} _{-0.05}	4716 ⁺³⁹ ₋₂₈	0.81 ^{+0.04} _{-0.04}	0.90 ^{+0.04} _{-0.04}	0.377 ^{+0.006} _{-0.006}	0.11 ^{+0.07} _{-0.07}	(30)
NGTS-7Ab	0.68	75.5 ^{+3.0} _{-13.7}	1.38 ^{+0.13} _{-0.14}	3359 ⁺¹⁰⁶ ₋₈₉	0.48 ^{+0.03} _{-0.12}	0.61 ^{+0.06} _{-0.06}	0 (fixed)	0 (fixed)	(31)
TOI-148b	4.87	77.1 ^{+5.8} _{-4.6}	0.81 ^{+0.05} _{-0.06}	5990 ⁺¹⁴⁰ ₋₁₄₀	0.97 ^{+0.12} _{-0.09}	1.20 ^{+0.07} _{-0.07}	0.005 ^{+0.006} _{-0.004}	-0.24 ^{+0.25} _{-0.25}	(32)
KOI-189b	30.36	78.0 ^{+3.4} _{-3.4}	1.00 ^{+0.02} _{-0.02}	4952 ⁺⁴⁰ ₋₄₀	0.76 ^{+0.05} _{-0.05}	0.73 ^{+0.02} _{-0.02}	0.275 ^{+0.004} _{-0.004}	-0.12 ^{+0.10} _{-0.10}	(33)
TOI-587b	8.04	81.1 ^{+7.1} _{-7.0}	1.32 ^{+0.07} _{-0.06}	9800 ⁺²⁰⁰ ₋₂₀₀	2.33 ^{+0.12} _{-0.12}	2.01 ^{+0.09} _{-0.09}	0.051 ^{+0.009} _{-0.036}	0.08 ^{+0.11} _{-0.12}	(32)
TOI-746b	10.98	82.2 ^{+4.9} _{-4.4}	0.95 ^{+0.09} _{-0.06}	5690 ⁺¹⁴⁰ ₋₁₄₀	0.94 ^{+0.09} _{-0.08}	0.97 ^{+0.04} _{-0.03}	0.199 ^{+0.003} _{-0.003}	-0.02 ^{+0.23} _{-0.23}	(32)
EBLM-J0555-57Ab	7.76	87.9 ^{+4.0} _{-4.0}	0.82 ^{+0.13} _{-0.06}	6368 ⁺¹²⁴ ₋₁₂₄	1.18 ^{+0.08} _{-0.08}	1.00 ^{+0.14} _{-0.07}	0.090 ^{+0.004} _{-0.004}	-0.04 ^{+0.14} _{-0.14}	(34)(35)
TOI-681b	15.78	88.7 ^{+2.5} _{-2.3}	1.52 ^{+0.25} _{-0.15}	7440 ⁺¹⁵⁰ ₋₁₄₀	1.54 ^{+0.06} _{-0.05}	1.47 ^{+0.04} _{-0.04}	0.093 ^{+0.022} _{-0.019}	-0.08 ^{+0.05} _{-0.05}	(32)
OGLE-TR-123b	1.80	89.0 ^{+11.5} _{-11.5}	1.29 ^{+0.09} _{-0.09}	6700 ⁺³⁰⁰ ₋₃₀₀	1.29 ^{+0.26} _{-0.26}	1.55 ^{+0.10} _{-0.10}	0 (fixed)	-	(36)
TOI-694b	48.05	89.0 ^{+5.3} _{-5.3}	1.11 ^{+0.02} _{-0.02}	5496 ⁺⁸⁷ ₋₈₁	0.97 ^{+0.05} _{-0.04}	1.00 ^{+0.01} _{-0.01}	0.519 ^{+0.001} _{-0.001}	0.21 ^{+0.08} _{-0.08}	(37)
KOI-607b	5.89	95.1 ^{+3.3} _{-3.4}	1.09 ^{+0.09} _{-0.06}	5418 ⁺⁸⁷ ₋₈₅	0.99 ^{+0.05} _{-0.05}	0.92 ^{+0.03} _{-0.03}	0.395 ^{+0.009} _{-0.009}	0.38 ^{+0.08} _{-0.09}	(12)
J1219-39b	6.76	95.4 ^{+1.9} _{-2.5}	1.14 ^{+0.07} _{-0.05}	5412 ⁺⁸¹ ₋₆₅	0.83 ^{+0.03} _{-0.03}	0.81 ^{+0.04} _{-0.02}	0.055 ^{+0.000} _{-0.000}	-0.21 ^{+0.07} _{-0.08}	(23)
TIC-320687387 B	29.77	96.2 ^{+1.9} _{-2.0}	1.14 ^{+0.02} _{-0.02}	5780 ⁺⁸⁰ ₋₈₀	1.08 ^{+0.03} _{-0.03}	1.16 ^{+0.02} _{-0.02}	0.366 ^{+0.003} _{-0.003}	0.30 ^{+0.08} _{-0.08}	(38)
OGLE-TR-122b	7.27	96.4 ^{+9.4} _{-9.4}	1.17 ^{+0.23} _{-0.13}	5700 ⁺³⁰⁰ ₋₃₀₀	0.98 ^{+0.14} _{-0.14}	1.05 ^{+0.20} _{-0.09}	0.205 ^{+0.008} _{-0.008}	0.15 ^{+0.36} _{-0.36}	(39)
TOI-1213b	27.22	97.5 ^{+4.4} _{-4.2}	1.66 ^{+0.78} _{-0.55}	5590 ⁺¹⁵⁰ ₋₁₅₀	0.99 ^{+0.07} _{-0.06}	0.99 ^{+0.04} _{-0.04}	0.498 ^{+0.003} _{-0.002}	0.25 ^{+0.13} _{-0.14}	(32)
K2-76b	11.99	98.7 ^{+2.0} _{-2.0}	0.89 ^{+0.05} _{-0.03}	5747 ⁺⁷⁰ ₋₆₄	0.96 ^{+0.03} _{-0.03}	1.17 ^{+0.06} _{-0.03}	0.255 ^{+0.007} _{-0.007}	0.01 ^{+0.04} _{-0.04}	(40)
CoRoT-101186644	20.68	100.6 ^{+11.5} _{-11.5}	1.01 ^{+0.25} _{-0.06}	6090 ⁺²⁰⁰ ₋₂₀₀	1.20 ^{+0.20} _{-0.20}	1.07 ^{+0.07} _{-0.07}	0.402 ^{+0.006} _{-0.006}	0.20 ^{+0.20} _{-0.20}	(41)
J2343+29Ab	16.95	102.7 ^{+7.3} _{-7.3}	1.24 ^{+0.07} _{-0.07}	5150 ⁺⁹⁰ ₋₆₀	0.86 ^{+0.10} _{-0.10}	0.85 ^{+0.05} _{-0.05}	0.161 ^{+0.002} _{-0.002}	0.07 ^{+0.01} _{-0.01}	(42)
EBLM-J0954-23Ab	7.57	102.8 ^{+5.9} _{-6.0}	0.98 ^{+0.17} _{-0.17}	6406 ⁺¹²⁴ ₋₁₂₄	1.17 ^{+0.08} _{-0.08}	1.23 ^{+0.17} _{-0.17}	0.042 ^{+0.001} _{-0.001}	-0.01 ^{+0.14} _{-0.14}	(35)
KOI-686b	52.51	103.4 ^{+4.8} _{-4.8}	1.22 ^{+0.04} _{-0.04}	5834 ⁺¹⁰⁰ ₋₁₀₀	0.98 ^{+0.07} _{-0.07}	1.04 ^{+0.03} _{-0.03}	0.556 ^{+0.004} _{-0.004}	-0.06 ^{+0.13} _{-0.13}	(33)
TIC-2									

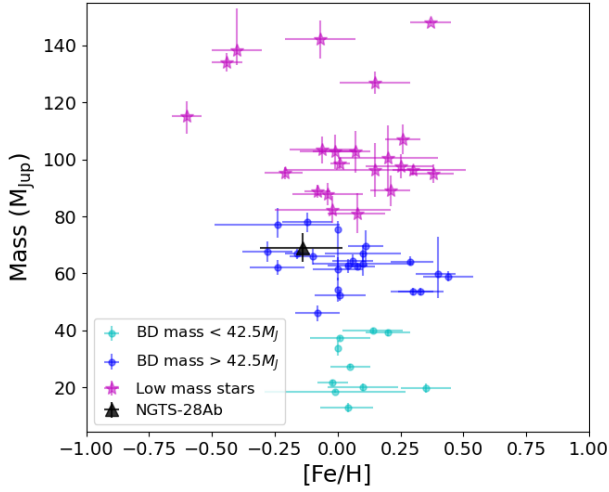


Figure A2. Mass-Metallicity plot of objects in A1. The metallicity is for the host star in each system. NGTS-28Ab is plotted as a black triangle. Low mass stars are plotted as magenta stars. BDs with masses above $42.5 M_{\text{J}}$ are dark blue circles and BDs with below $42.5 M_{\text{J}}$ are light blue circles. RIK-72b (David et al. 2019) and the binary system discovered by Stassun et al. (2006) are not included due to their youth.

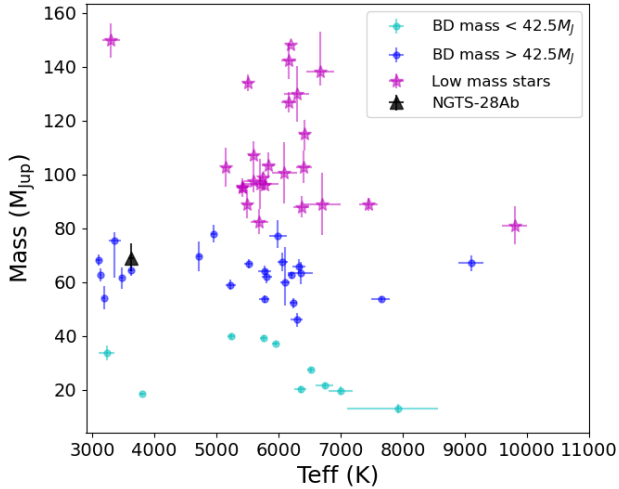


Figure A3. Mass- T_{eff} plot of objects in A1. The T_{eff} values are for the host star in each system. NGTS-28Ab is plotted as a black triangle. Low mass stars are plotted as magenta stars. BDs with masses above $42.5 M_{\text{J}}$ are dark blue circles and BDs with below $42.5 M_{\text{J}}$ are light blue circles. RIK-72b (David et al. 2019) and the binary system discovered by Stassun et al. (2006) are not included due to their youth.